Department of Applied Mathematical
and Physical Sciences,
National Technical University of Athens.

National Centre
for Scientific Research
Demokritos.

INTERDEPARTMENTAL MASTER'S DEGREE: PHYSICS AND TECHNOLOGICAL APPLICATIONS

Mapping the planetary nebula NGC 3242 with MUSE: SATELLITE spectroscopic view

Lydia Konstantinou

Research Supervisor:
Stavros Akras,
Associate Researcher

Academic Supervisor:
George Koutsoumpas,
Professor

Athens 2023

Η παρούσα διπλωματική εργασία πραγματοποιήθηκε σε συνεργασία με το Ινστιτούτο Αστρονομίας, Αστροφυσικής, Διαστημικών Εφαρμογών και Τηλεπισκόπησης του Εθνικού Αστεροσκοπείου Αθηνών.

This master's thesis has been carried out in collaboration with the Institute for Astronomy, Astrophysics, Space Applications and Remote Sensing of the National Observatory of Athens.

https://www.astro.noa.gr
https://www.noa.gr

Περίληψη

Τα Πλανητικά Νεφελώματα (ΠΝ) είναι το αποτέλεσμα των ισχυρών αστρικών ανέμων που επικρατούν προς το τέλος της ζωής των αστέρων μικρής και μεσαίας μάζας. Το νεφέλωμα ιονίζεται από την εκπεμπόμενη υπεριώδη ακτινοβολία του κεντρικού αστέρα και τελικά λαμβάνει μία ομοιογενής δομή. Ωστόσο, σε ορισμένα ΠΝ υπάρχουν δομές χαμηλού ιονισμού (LISs) ενσωματωμένες στις κύριες δομές, η φύση των οποίων είναι ελάχιστα κατανοητή. Ο σκοπός της παρούσας διπλωματικής εργασίας, είναι η φασματοσκοπική ανάλυση του ΠΝ NGC 3242 στο οποίο παρατηρούνται και οι προαναφερθείσες μικρό-δομές. Με τη χρήση του κώδικα SATELLITE μελετήσαμε τη χημική σύσταση του ΠΝ ψάχνοντας για πιθανές διακυμάνσεις των φυσικών παραμέτρων με ιδιαίτερη έμφαση στην περιοχή των LISs. Καταλήξαμε ότι δεν υπάρχει σημαντική διακύμανση των αφθονιών ενώ η ηλεκτρονιακή πυκνότητα και θερμοκρασία δεν παραμένουν σταθερές. Επίσης, το NGC 3242 φαίνεται πως είναι ένα νεφέλωμα χαμηλού ιονισμού και ότι τα LISs δεν έχουν προκληθεί από κάποιο σοκ. Επιπλέον, τα ακτινικά προφίλ ορισμένων τυπικών γραμμών εκπομπής επιβεβαίωσαν ότι οι γραμμές χαμηλού ιονισμού έχουν τις μέγιστες τιμές τους στα LISs, όπως αναμενόταν. Τέλος, η λεπτομερής εξέταση των δεδομένων του MUSE οδήγησε στον εντοπισμό της γραμμής εκπομπής [C I] λ8727 η οποία μάλιστα εκπέμπεται μόνο από τα LISs. Αυτό το αποτέλεσμα υποδηλώνει ένα μερικώς ιονισμένο αέριο που μπορεί να περιβάλλει ένα πυκνό μοριακό αέριο. Η βασική μας ανάλυση στηρίχτηκε σε δεδομένα από το φασματογράφο Multi Unit Spectroscopic Explorer (MUSE), του Very Large Telescope (VLT), ενώ χρησιμοποιήθηκαν και δεδομένα από το διαστημικό τηλεσκόπιο Spitzer.

Abstract

A planetary nebula (PN) is formed when a low-to-intermediate mass star, passes the final stages of its evolution and ejects its outer envelopes due to strong stellar winds. The UV radiation from the central star of a planetary nebula, ionises the gas, leading to a homogeneous ionisation structure of the nebula. However, some PNe display Low Ionisation Structures (LISs) embedded in the outer structures, and although there are some theoretical scenarios about their origin, their nature still remains poorly understood. The aim of our analysis is to make a thorough spectroscopic analysis of the multiple shell PN NGC 3242, which also contains the aforementioned microstructures. Our analysis is mainly based on the SATELLITE code, which was used to study the chemical composition of the PN and test the variation of the physical parameters throughout the nebula, with a particular interest for the LISs. This analysis proved that there is no chemical variation throughout the nebula, while the electron density and temperature varies between the nebular structures. At the same time, the diagnostic diagrams revealed that NGC 3242 is a low ionised nebula and that the LISs aren't shock excited regions. Besides, the radial profiles of some typical emission lines confirmed that the low ionisation lines peak at the LISs as it was expected. Last but not least, our detailed examination of MUSE data has led to identify the [C I] λ8727 emission line emitted only from the LISs. This finding implies a partially ionised gas which may surrounds a dense molecular gas. For our analysis, we used data-cubes from MUSE at VLT, which is an Integral Field Unit (IFU) operating in the visible range of the spectrum. Additionally, we are using infrared data from Spitzer Space Telescope and examine their radial profiles.

Θα ήθελα πρώτα να ευχαριστήσω τον κ.Σταύρο Άκρα που με βοήθησε τόσο να εκπονήσω τη μεταπτυχιακή μου εργασία καθώς και τον κ.Γεώργιο Κουτσούμπα για τη βοήθεια του. Θα ήθελα, επίσης, να ευχαριστήσω τον Κωνσταντίνο Μπουβή για τη συνεργασία και τη συμβολή του στην παρούσα εργασία. Τέλος, θέλω να εκφράσω ένα μεγάλο ευχαριστώ στην οικογένειά μου και στους φίλους μου που με στηρίζουν και με ενθαρρύνουν. Είμαι βαθύτατα ευγνώμων για την αμέριστη αγάπη και εμπιστοσύνη που μου δείχνουν.

–Λυδία Κωνσταντίνου

I would like to first thank Dr. Stavro Akra for his invaluable assistance in completing my master thesis, as well as Prof. George Koutsoumba for his help. I would also like to express my gratitude to Konstantinos Bouvis for his collaboration and contribution to this work. Finally, I owe a big thank you to my family and friends who support and encourage me. I am deeply grateful for the unconditional love and trust they show me.

– Lydia Konstantinou

Contents

Figures catalogue

Chapter 1

Introduction

1. Stellar evolution

1.1. Protostar formation

Although the space between stars seems to be empty, in fact it consists of huge amounts of gas and dust. The combination of these defines the Interstellar Medium or ISM. ISM is mainly made from Hydrogen, a small percentage of heavier elements and dust. Molecular clouds, with sizes of few light years, can be created in this mixture of gas and dust. Within these molecular clouds, tight clumps of gas and dust give birth to stars.

The procedure for the formation of protostars begins when clumps are dense enough, and they collapse under their own gravity. The collapse begins when the gas, triggered by some disturbance, such as the collision of two molecular clouds or the shock wave from nearby supernovae. The next step is the fragmentation of the cloud into smaller regions, which contracts to form stellar nuclei. At the same time, the cloud heats up due to the conversion of gravitational potential energy into thermal energy, leading to an increase in pressure at the centre of the cloud. This procedure eventually leads to the formation of a protostar. On the HR diagram the protostars follow the Hayashi track which is almost a vertical curve. The mass and chemical composition of the star affect the exact form and location of the Hayashi track on the Hertzsprung-Russell diagram. For instance, for solar masses stars, the Hayashi track is located

at a temperature of about $4000K$.

After the formation of the protostar, the gas starts rotating with very high speed, leading to higher temperatures and causing the flattening of the cloud. At this stage, the protostar is surrounded by a protoplanetary disk, which contains all the necessary materials to later form planets. In addition, as the protostar rotates it generates a powerful magnetic field which creates a strong protostellar wind, i.e. an outflow with particles. Additionally, many protostars release gas into space in the form of fast streams or jets. The more the protostar grows, the stronger the gravitational pull becomes, and more material is accumulated and so on.

At the same time, the protostars fuse Deuterium, which consists of a neutron and a proton at its nucleus. This procedure keeps the temperature of the protostar constant at 10^6K. The fusion creates radiation pressure which counterbalances the pull of gravity, leading to a stable state for the protostar. The protostar's interior is cooler than a regular star's and this is the reason why they can't fuse Hydrogen atoms.

If the central temperature of the contracted protostar increases enough, then the nuclear reactions finally start. At this point, the creation of a new star begins. Up until Deuterium fusion stops, stars like the Sun reduce their size under a constant temperature. The young stars heat up with a relatively constant brightness and once the burning of Hydrogen begins, the gravitational contraction stops. The stars then move in the zero age main sequence on the HR diagram (Hannu Karttunen, 2017; Kaler, 2020; Kwok, 2000).

1.2. Main sequence phase

The main sequence is the phase where a star spends the 90% of its life. While the stars are in this phase, they convert Hydrogen into Helium through thermonuclear reactions in their cores. In order to achieve this conversion, stars use two basic mechanisms:

- The proton-proton chain
- The CNO cycle

In the first case, two Hydrogen nuclei create a chemical bond to form a Deuterium nucleus. At the same time, a positron and a neutrino are released. Subsequently, the Deuterium nucleus and a new Hydrogen nucleus are fused and as a result, Helium-3 is created. Also, through the fusion, a photon is released and escapes carrying energy. Finally, two Helium-3 nuclei are combined to create a Helium-4 as well as two protons. Below all the aforementioned chemical reactions are listed.

$$
\begin{aligned}
{}^{1}\mathrm{H} + {}^{1}\mathrm{H} &\longrightarrow {}^{2}\mathrm{H} + e^{+} + \nu \\
{}^{2}\mathrm{H} + {}^{1}\mathrm{H} &\longrightarrow {}^{3}\mathrm{He} + \gamma \\
{}^{3}\mathrm{He} + {}^{3}\mathrm{He} &\longrightarrow {}^{4}\mathrm{He} + {}^{1}\mathrm{H} + {}^{1}\mathrm{H}
\end{aligned}
$$

This is the primary mechanism for energy generation in stars like the Sun, accounting for approximately 99% of its energy output. The proton-proton chain is highly temperature-dependent and higher temperatures mean faster fusion rates resulting to greater energy production. The core of the Sun reaches temperatures exceeding 15 million degrees Celsius and pressures exceeding 250 billion times the atmospheric pressure, creating the conditions necessary to sustain the chain reaction.

The CNO cycle relies on the presence of Carbon, Nitrogen, and Oxygen isotopes to catalyse the fusion of four protons into a helium nucleus. Both gamma rays, which are emitted from the star's core, and neutrinos, which leave the star without interacting with matter, are produced by this process. Each one of the isotopes is used at a different step of the CNO cycle, and it is recreated in a later stage. The final product is an alpha particle, namely a stable Helium nucleus, two positrons and two neutrinos. So, the reactions occurring during a CNO cycle are the following:

$$
\begin{aligned}
{}_{6}\mathrm{C}^{12} + {}_{1}\mathrm{H}^{1} &\longrightarrow {}_{7}\mathrm{N}^{13} + {}_{0}\gamma^{0} \\
{}_{7}\mathrm{N}^{13} &\longrightarrow {}_{6}\mathrm{C}^{13} + {}_{1}\mathrm{e}^{0} + {}_{0}\nu^{0} \\
{}_{6}\mathrm{C}^{13} + {}_{1}\mathrm{H}^{1} &\longrightarrow {}_{7}\mathrm{N}^{14} + {}_{0}\gamma^{0} \\
{}_{7}\mathrm{N}^{14} + {}_{1}\mathrm{H}^{1} &\longrightarrow {}_{8}\mathrm{O}^{15} + {}_{0}\gamma^{0} \\
{}_{8}\mathrm{O}^{15} &\longrightarrow {}_{7}\mathrm{N}^{15+}{}_{1}\mathrm{e}^{0} + {}_{0}\nu^{0} \\
{}_{7}\mathrm{N}^{15} + {}_{1}\mathrm{H}^{1} &\longrightarrow {}_{6}\mathrm{C}^{12} + {}_{2}\mathrm{He}^{4}
\end{aligned}
$$

The CNO cycle requires very high temperatures and densities to support the reactions, but it is a more efficient source of energy than the proton-proton chain, releasing more energy per reaction. This procedure is used from heavier stars for energy production because it demands higher core

temperature and pressure to be initiated. By this procedure, He and H are converted to heavier elements. These elements can be used in later stages for the formation of even heavier elements, like Iron, releasing enormous amounts of energy.

Generally, the evolution of a star depends on its mass. This is reasonable because the mass represents the amount of energy a star can produce and how quickly the energy is generated (Kaler, 2020). At the same time, the more massive the star is, the bigger its internal pressure and its temperature are. In addition, since the burning of Hydrogen is a highly temperature sensitive process, a small increase in mass implies a rapid increase in the burning rate of Hydrogen. Higher stellar mass means higher neuclear-burning core mass, resulting in more fuel supply. Nevertheless, the increased rate of Hydrogen fusion can counterbalance this fuel supply, thereby shortening the lifetime of the star.

The luminosity (L), which represents the fusion rate, is linked to the stellar mass via the relation:

$$L \propto M^{3.5} \tag{1.1}$$

In particular, from the equation 1.1 we can deduce how much time a star will spend in the main sequence as a function of its mass:

$$t \propto M^{-2.5} \tag{1.2}$$

From the above, specifically from the equation 1.2, the conclusion is that the more massive the star is, the sooner it leaves the main sequence, because its energy supplies come to an end more quickly. The massive stars burn their Hydrogen through CNO cycle and by this mechanism the Hydrogen is burning fast. On the other hand, stars with smaller masses stay longer in the main sequence because they consume their Hydrogen more slowly via the proton-proton chain mechanism (H.Shu, 2017). Also, from the equation 1.1 it is obvious that the smaller stars are less luminous.

Finally, the main sequence stars are divided into three different main categories according to their masses. The first one, consists of stars with masses smaller than $0.8\,M_{\odot}$ (Kaler, 2020). Such small masses prevent stars from evolving further. The second category contains stars with masses between $0.8\,M_{\odot}$ and $9\,M_{\odot}$ (Kaler, 2020). These stars, after billions of years, eventually die and form white dwarfs. For instance, the sun is an intermediate-mass star which will stay at the main sequence for about

another 4.5 billion years. The final category includes the more massive stars, which end their lives in a supernova explosion. The remnants of such explosions can either be a neutron star or a black hole, and the specific outcome depends on the mass of the star. It is worth mentioning that up to the red giant stage, both intermediate and high mass stars follow the same path on the HR diagram (H.Shu, 2017; Hannu Karttunen, 2017).

1.3. After the main sequence phase

When a star runs out of Hydrogen, it can no longer produce nuclear energy to counterbalance gravity, so it leaves the main sequence. An intermediate-mass star now moves right on the HR diagram, where the Red Giants are located (Figure 1.1). At this phase, the star is bigger and more luminous. As for high-mass stars, they also move to the right, but

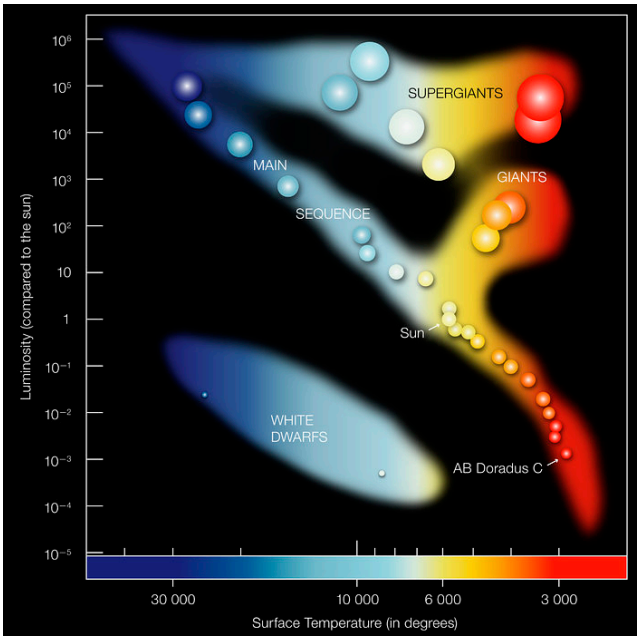

Figure 1.1: The temperatures of stars are displayed against their luminosities on the Hertzsprung-Russell diagram. A star's location in the diagram reveals details about its current stage and mass. On the diagonal branch, often known as the main sequence, stars that fuse hydrogen into helium are located (Credit: ESO).

they become Supergiants (SRG), which are bigger and more luminous

than red giants (Figure 1.1). Also, as the stars turn into supergiants, their surface cools down.

Both at the red giant phase and supergiant phase the gravity prevails over internal pressure, causing the core to shrink, which results in an increase in temperature and density. On the contrary, the outer parts of the star expand (H.Shu, 2017). Eventually, the overall size of the star becomes bigger than before, and the temperature is lower than the previous evolutionary stage.

After this stage, the evolution of stars and the path that they will follow on the HR diagram differ dramatically. Eventually, the star will reach the end of its life, leaving behind one of the three known stellar corpses, namely white dwarfs, neutron stars and black holes (Kaler, 2020).

1.3.1. Intermediate-mass stars

After the main sequence the stars up to $5\,M_{\odot}$ in comparison with the stars with masses between $5\,M_{\odot}$ and $8\,M_{\odot}$, follow a slightly different path. At lower-mass stars when the temperature of the nucleus rises to 100 million K, they consist of a Helium-burning core, while a Hydrogen fusing shell surrounds the core (H.Shu, 2017). If the core temperature exceeds 300 million degrees K, an almost explosive consumption of Helium takes place. The Helium flash, as it is called, is responsible for the production of Carbon in the core, which is generated through triple-alpha reactions.

$$^{4}\mathrm{He} + {}^{4}\mathrm{He} \longleftrightarrow {}^{8}\mathrm{Be}$$
$$^{8}\mathrm{Be} + {}^{4}\mathrm{He} \longrightarrow {}^{12}\mathrm{C} + gamma\,ray$$

For stars that never reach these high temperatures, the burning of Helium starts more quietly. The Helium-burning core that is surrounded by a Hydrogen-fusing shell expands and its temperature decreases. In parallel, the temperature of the upper layers, the thermal pressure and the radius of the photosphere decrease. The star now retreats about halfway down the Red Giant Branch (RGB). By this movement, the horizontal branch on the HR diagram takes place. The exact position in which the star will end up in the horizontal branch depends on its mass, its

chemical composition, and the percentage of mass that was lost during the preceding expansion stages. From $5\,M_{\odot}$ and above, the evolution proceeds similarly, but instead of settling into a distinct position on the HR diagram, the stars return to higher temperatures, where they can fuse Helium.

When the fusion of Helium is completed, the star's core is mainly composed of Carbon and Oxygen. As for its outer parts, there is a first shell of Helium around the core and the shell itself is also surrounded by a Hydrogen-burning shell. The core shrinks again, unlike the outer parts, which expand. The star is getting cooler and more luminous. On the HR diagram, the star is moving up-right and its path is almost aligned with the previous path of the red giant phase, hence the name Asymptotic Giant Branch (AGB) of this stage. At the early-AGB, the Hydrogen shell is getting fainter, and finally it disappears due to the envelope's expansion. After that, the thermal-pulsing AGB begins and the H reignites in a thin shell (Kwok, 2000). Strong stellar winds are present in this phase, leading to mass loss, which is responsible for the ending of AGB. This process enriches the initially cold gas with molecules and elements, derived from the star's outer layers. Much of the Carbon, most of the Nitrogen, and significant fractions of other elements in the Interstellar Medium come from such winds Kaler (2020).

This sets the stage for post-AGB evolution toward the PN phase. Mass loss from the surface, also, prevents the core to get big enough and ignite Carbon, and therefore it allows stars with initial masses as high as $8\,M_{\odot}$ to become White Dwarfs (WDs). Planetary nebulae (PN) are also created at the end of AGB. So, WDs are the central stars of planetary nebulae (CSPN) and their core mass must be from $0.55\,M_{\odot}$ to $0.64\,M_{\odot}$ (Kwok, 2000). At first, WDs evolve with approximately constant luminosity. While the mass decreases, the luminosity also drops and the WDs move downward to the cooling tracks on the HR diagram (see Figure 1.2 for the movement of the star on the HR diagram).

1.3.2. High-mass stars

After the main sequence, a high-mass star goes into the supergiant phase. Also, in the case of more massive stars, burning of Helium begins under non-degenerate conditions. This implies that no Helium-flash occurs, and the star does not cross the horizontal branch. After the core runs

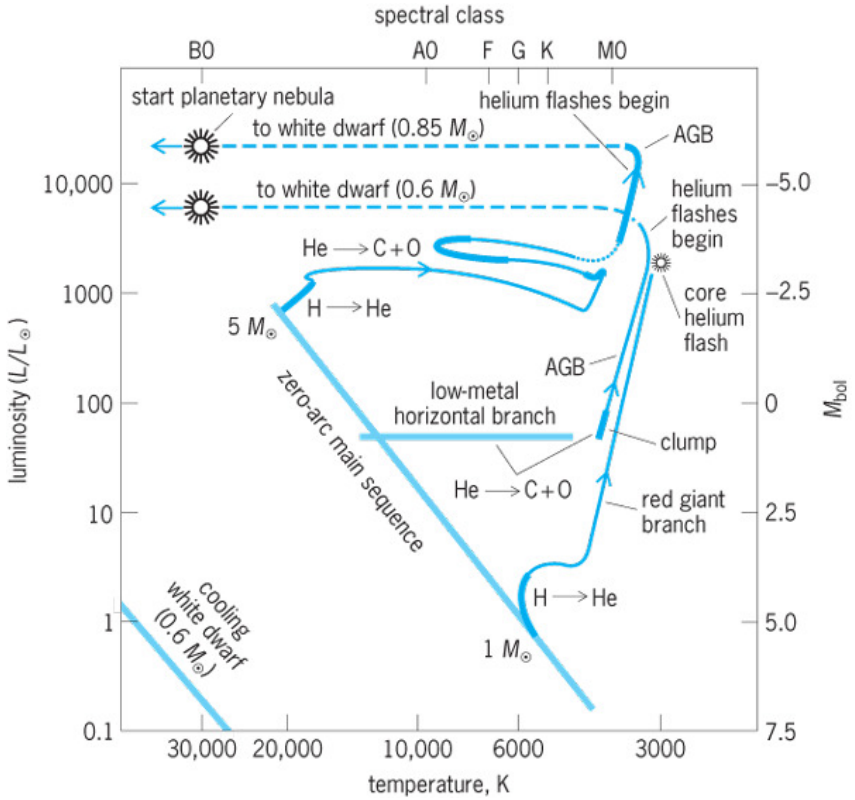

Figure 1.2: The evolution of an intermediate mass star on the HR diagram.

out of Helium, nuclear fusion continues to form heavier elements until the core is mostly iron.

At this stage, the star runs out of energy supplies and its fate is a destructive explosion. The iron cannot be burned to produce heavier elements, nor can provide more energy in any other way. As the star's core begins to contract, its temperature increases and consequently endothermic nuclear reactions are favoured. The photodissociation of the iron begins according to the equation:

$$26Fe^{56} + h\nu \rightarrow 132He^{4} + 4n$$

Subsequently, the produced helium decay. The above reactions absorb energy and consequently accelerate the collapse of the star. In the final stage, electron capture reactions occur.

$$p^{+} + e^{-} \rightarrow n + \nu_e$$

The neutrinos released by these reactions carry huge amounts of energy out of the core. In each layer, the pressure cannot overcome the

gravitational force. Inevitably, the star collapses under its own gravity in a catastrophic event which is called type II supernova explosion, and is one of the most energetic events in the universe. During this explosion, heavy stars release an enormous amount of energy and matter, including elements heavier than Iron, into the interstellar medium.

At the same time, a powerful shock wave propagates outward, while a very dense body remains at the core of this explosion. Depending on the mass of the remaining core and its chemical composition, the remnant will be a neutron star or a black hole. If the mass isn't high enough, the neutrons released during photolysis accumulate in the core, creating a neutron star. The pressure inside the neutron star is so strong that it manages to resist the total gravitational collapse. Therefore, there is an upper limit for neutron stars' mass, which is $M_{OVS} \approx 3.2 M_{\odot}$. So, if after the explosion a mass greater than $3.2\,M_{\odot}$ accumulates in the core, then the gravity is so strong that a complete gravitational collapse occurs, resulting in the creation of a black hole (Kaler, 2020; H.Shu, 2017).

2. White dwarfs

White dwarfs are the product of the interception of the gravitational collapse of a common star by the pressure of degenerate electrons. If the mass of the star is smaller than $1.44\,M_{\odot}$, the above balance is achieved. This mass limit is known as Chandrasekhar limit in honour of the Astrophysicist Subrahmanyan Chandrasekhar, who proved that the mass of a white dwarf can't overcome the 1.44 solar masses, according to the mathematical relation:

$$M_{ch} = 0.20 \left(\frac{Z}{A}\right)^2 \left(h \frac{c}{G\ m_p^2}\right)^{\frac{3}{2}} m_p\,, \tag{1.3}$$

where c is the speed of light, A is the mass number, Z is the atomic number, h is the Planck's constant, G is the gravitational constant and finally m_p is the proton's mass. A white dwarf has approximately the Earth's size, but its mass is $M \approx 0.7 M_{\odot}$. Additionally, the mean temperature of a white dwarf is between $10^6 K$ and $10^7 K$. As for its density, is about $10^6 gr\ cm^{-3}$.

The first white dwarf that was ever discovered, was the Sirius B,

which is the companion star of Sirius. The paradox nature of Sirius B wasn't understood until the 1915 when it was found to have a surface temperature of 25,000 K. This fact means that it was ejected from the star enormous amounts of energy per surface unit. However, Sirius B was ten thousand times fainter than its companion star (Kwok, 2000). Also, its temperature was significantly high, given that its mass was about $1\,M_{\odot}$. The combination of the above observations led to the conclusion that Sirius B must have a diameter slightly smaller than the Earth's. So, it was a small star with high mass which resulting in a very high density.

The chemical composition of a white dwarf mainly depends on the mass of the progenitor star. Specifically, if the initial mass of the star was bigger than Sun's mass, then the nuclear fusion will produce Magnesium, Neon and a small amount of Oxygen. As a result, the white dwarf will consist mainly of these elements. A star with mass equal or smaller than one solar mass, it doesn't have enough energy to proceed with the fusion of Carbon, so the white dwarf that will remain after the death of the star, it will mainly consists of Carbon and Oxygen. Finally, a star with less than half the mass of the Sun will never fuse even the Helium, and will therefore leave behind a white dwarf composed mostly of Helium.

White dwarfs are found alone or in binary systems. Also, it is remarkable that white dwarfs don't have inner energy sources and the further gravitational contraction is prevented by the pressure of the degenerate electron gas. Therefore, by emitting their remaining thermal radiation, white dwarfs gradually become cooler. During this cooling process their colour change too from white to red and finally black. However, the cooling rate of a white dwarf is comparable to the age of the Universe so, even the oldest ones are observable today (Kwok, 2000).

3. Planetary Nebulae

The first planetary nebula was discovered in 1764 by Charles Messier while their misleading name, was given by William Herschel (Kwok, 2000). Due to the deficient resolution of the telescopes at that time, the scientists thought that planetary nebulae were identified with greenish disks around planets. Today, we know that this assumption is wrong. They finally were distinguished from other nebula by their structure and

their relation with a central star. This distinction became even clearer with spectroscopy.

Unlike the continuum spectra of stars, the spectrum of PNe is composed of emission lines. So, since planetary nebulae have a completely different spectrum than stars, their brightness must come from other mechanisms. The idea that PNe derive their energy from a nearby star with high temperature, was first considered by Herschel (1791) (Kwok, 2000).

In the 1956, Shklovsky was the first who proposed that PNe are the ancestors of white dwarfs and the progenitors of red giants (Kwok, 2000). The Interacting Stellar Winds (ISW) model, which was proposed by Kwok et al. (1978), suggests that PNe are formed from the interaction of strong stellar winds with material ejected from low-mass stars during the AGB. So, PNe aren't the result of a single event of mass loss, but they represent a rearrangement of material ejected over a long period of time (Kaler, 2020). When the central star is hot enough, a new phase of mass loss begins. The star's radius is now considerably lower than it was during the AGB, thus, the wind's velocity will be significantly higher. A high-density shell will be created when this new, high-speed wind collides with the remnant of the ABG cold wind. At the same time, the warm core of the star radiates in the ultraviolet part of the electromagnetic spectrum, resulting in the ionisation of the surrounded gas. At the end, a white dwarf will remain at the centre of the planetary nebula.

Planetary nebulae are approximately 10^{24} times less dense than Earth's atmosphere and their density varies from younger to older PNe. The younger PN are denser and while they are growing up they are getting less and less dense. A planetary nebula expands at a rate of 10–30 km/s (Schönberner et al., 2018). This means that after 10,000–50,000 years it will be so large and diffuse that it will have spread into the interstellar medium. As for the size of planetary nebulae, their typical diameters are about 1 light year and their masses are between $0.1\,M_{\odot}$ and $1\,M_{\odot}$. The central star of a planetary nebula, reaches temperatures up to 200,000 K and its radiation heats the gas to temperatures about 10,000 K. Moreover, due to the decrease in density through time, the emission of PNe decreasing as well. Eventually, they become unobservable, with mean lifetimes approximately 10^4 years. In addition, because of the high stellar temperatures, PNe are very high ionised nebula.

As for the abundances of planetary nebulae it is assumed that they are connected to the mass of the central star (Kwok, 2000) and based on

that, four different categories of PNe were proposed by Peimbert (1978). The first category is the Type I PNe, which are rich in He and N, and they usually show bipolar structure (we are going to analyse the morphological structures in a following section). The PNe that belong in this category, it is assumed that they are generated from high-mass population. The second and third type, Type II and III, consists of PNe that are located in the Galactic plane. The final category, Type IV, are halo objects that follow a sequence of decreasing initial mass and increasing age.

Lastly, PNe are ideal laboratories for the study of interactions between radiation and matter. More specific, they are mainly simple systems consisting of a central star feeding energy to the surrounding nebula. Also, they play an important role in the chemical evolution of galaxies. PNe return material to interstellar space, contributing to the enrichment with heavy elements such as carbon and oxygen. It is clear, therefore, that the study of planetary nebulae is of particular importance.

3.1. Spectrum of Planetary Nebulae

The main energy source of a planetary nebula is the white dwarf at its centre. The ultraviolet radiation from the central star removes electrons from the atoms at the gas and causes the ionization of these atoms. By this procedure, which is known as photoionization, the free electrons from the ionized atom, carries enough energy for the collisional excitation of heavy atoms. Spontaneous emissions from the excited states of these atoms, resulting in an emission line spectrum.

The collisional excitation demands the energy gaps between the excited states and the ground state to be small. Heavy atoms can be excited from collisions because this gap isn't significant. On the other hand, in the matter of He and H these energy gaps are notable, and the atoms cannot be collisionally excited. For instance, the energy gap between the first excited state and the ground state for Hydrogen, is at the 13.6 eV. This energy corresponds to an excitation temperature around $10^5 K$ which is much higher than the mean temperature of a planetary nebula. Nevertheless, even the electrons which can overcome this energy gap, cannot cause the excitation of H by collisions due to the low densities of PN. So, the excitation mechanism for He and H is the recombination between free electrons and protons.

The optical spectrum of a PN is dominated by emission lines (see Figure 1.3) and a weak component of continuum resulting from recombination processes and collisions (Akras, 2010). In the following subsections, I analyse in more detail the mechanisms that create the emission lines as well as the continuum in the spectra of planetary nebulae.

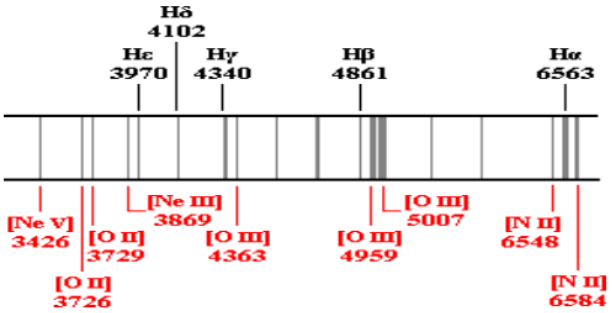

Figure 1.3: The typical optical spectrum of a planetary nebula.

3.1.1. Collisionally excited lines

Although the abundances of heavier atoms in a planetary nebula are lower than the abundance of Hydrogen, the collisional processes are several orders of magnitude faster than the recombination processes. As a result, the collisional excited lines are strong.

The emission lines, that comes from collisions, are called forbidden lines. They called "forbidden lines" because they don't exist under normal conditions on Earth, where gases are denser than the gas of a nebula. A forbidden line is produced when an electron moves from an upper energy level to a lower level through a radiative transition. This transition requires a long time to take place, so in Earth's atmosphere the excited atom would collide long before it could radiate its energy away. However, in regions of low density, collisions between particles are extremely rare. This provides enough time for spontaneous decay to take place.

On top of that, all these transitions violate the LS coupling, because they are not consistent with the selection rule: $\Delta l = \pm 1$. This selection rule implies that since the emitted photon carries angular momentum, at least one electron must change its angular momentum (Kwok, 2000). In conclusion, the forbidden transitions, involve transitions within the same

configuration. These lines are indicated by square brackets. Some of the most important and strong forbidden lines in case of planetary nebulae are the emission lines of [O III] 5007 Å, 4363 Å, [N II] 6584 Å, 6548 Å and [S II] 6716 Å, 6731 Å.

3.1.2. Recombination lines

Since the Hydrogen or Helium atoms cannot be collisionally excited in a nebula, the only way to find them in an excited energy level, is by recombination. The UV photons from the central star, or nearby stars, transfer energy to the planetary nebula, via the photoionisation process. During this process, the photons with energy greater than 13.6 eV ionise the atoms of Hydrogen and Helium (Kwok, 2000). The thermal electrons, that produced by the photoionisation, are recaptured by ions and this procedure occurs only in excited levels. Finally, the excited atoms are moving to lower energy states by spontaneous emissions.

The recombination gives the HI-Balmer lines and Paschen lines that typically observed in gaseous nebulae. Some of the most important recombination lines are the Hα, Hβ, and Hγ as well as the line He I 4868 Å.

3.2. Continuum radiation

There are several mechanisms that contribute to the continuum spectra of a planetary nebula. The main source of the continuum in the visible region is the free-bound emission. This type of emission happens when an electron recombines with a proton forming an atom at an excited level, accompanied by the simultaneous emission of a photon.

Moving to the infrared region of the electromagnetic spectrum, the free-free emission becomes stronger than the free-bound. It is called, free-free emission because the electrons collide with protons without being captured. So, the electrons are free even after the interaction, but at the same time they slow down. The above results in a continuum radiation. The free-free continuum emission is also the main mechanism for the continuum spectra observed in radio.

Another interesting mechanism for continuum radiation is the two proton radiation. The deexcitation of Hydrogen atoms from the metastable

energy level 2s, resulting to this type of radiation. A photon can escape from this metastable level only by photoionization and collision transition from the 2p energy level, emitting a Lyman a photon. In low density nebula an atom can move from the 2s level to a virtual p state and then the electron can jump from this state to the ground state emitting two photons. The sum of the energies of these photons must be equal to 10.3eV, which is the energy of the Lyman a line.

Lastly, the central star of a PN emits radiation which then interact with dust grains in the surrounding nebula. The scattered radiation from the central star, contributes to the continuum radiation (Kwok, 2000).

3.3. Morphology of planetary nebulae

Planetary nebulae have a large variety of morphologies, and they are divided into different classes based on their appearances. Although, they are classified as stellar, disk, ring, irregular, bipolar, quadrupolar (García-Segura et al., 1999), and other types by different authors, there are three main types that we mainly use to describe them: spherical, elliptical and bipolar. These three main types are the results from the appearance of the main structures of PNe, while all the subtypes come from the smaller outer structures.

The vast majority of planetary nebulae aren't completely spherical. However, spherical PNe are formed by the slow and steady wind of a single asymptotic giant branch (AGB) star, which creates a dense shell of gas and dust around the star. The star sheds its outer layers when its fuel runs out, leaving behind a rounded shell that is lighted by the star's hot core. Elliptical planetary nebulae, on the other hand, are typically elongated. The fast hot wind coming from the central star is affected by the matter that is more concentrated in the equatorial region of the star, which causes the corresponding PNe to have elliptical or weakly bipolar shapes (Reimers et al., 2000). This model can explain a wide variety of elliptical shapes. Lastly, bipolar planetary nebulae have two lobes, or "wings", which are often perpendicular to each other. These nebulae are believed to be formed by the interaction of a fast wind from the AGB star with a slow and dense disk of gas and dust surrounding the star. The two lobes of the nebula are formed as a result of the rapid wind's collision with the disk, which generates two opposing shock fronts that sweep up the gas and dust.

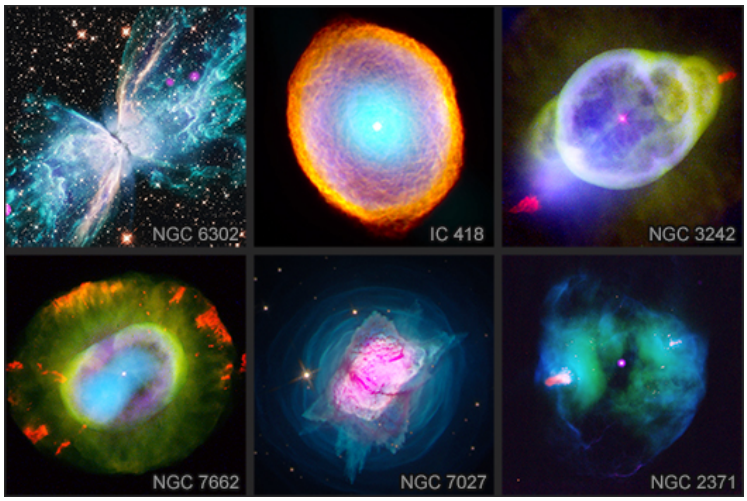

Figure 1.4: Planetary nebulae with a variety of shapes (X-ray: NASA/CXC/RIT/J.Kastner; Optical: NASA/ESA/AURA/STScI).

This variety of the different classes is partially a consequence of the projection effect, Figure 1.4 shows different shapes of PNe. More specific, when we observe a nebula from different angles, it will appear different. On top of that, the way that the gas was ejected initially from the central star to the space and its interaction with the ISM, perhaps resulting in different morphologies. It has also been shown that nebulae with more irregular shapes are produced by more massive stars. In addition, if at the centre of the PN exists a binary system of stars, gravitational interactions between the stars could cause different nebular shapes. Another theory is that during the formation of the nebula, planets may prevent the star to eject away matter.

As it was mentioned at the beginning of the section, the appearance of a PNe is also connected to its main structures. The Interaction of stellar winds, known as ISW model can explain the majority of them, like the halos, the shell and the bright rim (Gonçalves et al., 2001). Halos are the fossil of mass loss episodes during the AGB phase, and they are very faint (Monreal-Ibero et al., 2005). Not all planetary nebulae display a halo, but it has been observed at a percentage of 60% of the PNe with deep observations. Unlike the main body of PNe, halos are often spherical (Fang et al., 2018). On the other hand, the shells of PNe, which are mostly made of ionised gas and dust, represent the result from the interaction of the dying star with the interstellar medium (Phillips et al., 2009). As for the rim, it is a very bright and sometimes sharp-edged structure, which is created from the interaction of the cooler, neutral

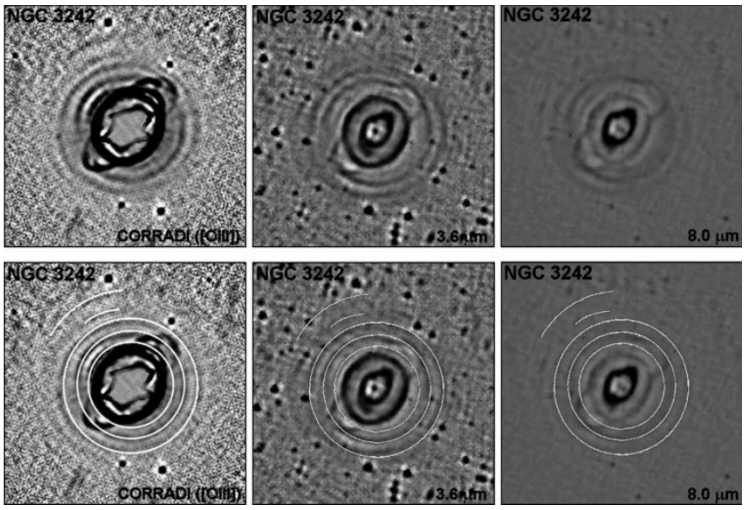

Figure 1.5: NGC 3242 from Spitzer Space Telescope and [O III] images taken from Corradi et al. (2004). In every image, the rings are observable.

gas in the interstellar medium with the ionised gas. So, it is the relic of early ionisation D-type fronts (Phillips et al., 2009). Lastly, in some PNe "rings" have been identified (see Figure 1.5), mainly from observations with Hubble Space Telescope (Corradi et al., 2004). Some of the models that have been proposed about their formation, include interaction of binary systems, magnetic activity cycles, instabilities in dust-winds and stellar oscillations. Nevertheless, little is known about these structures (Corradi et al., 2004).

Nevertheless, except of the main structures of PNe there are also many microstructures which can be found at the outer parts of PNe. These structures are mainly seen in the light of low ionisation lines like the forbidden lines of [S II] or [N II] and they are known as Low Ionisation Structures (LISs) (Akras et al., 2017). Also, observations in several PNe have revealed the existence of molecular Hydrogen in LISs with significant densities. However, until now doesn't exist a general rule which can explain how the molecular Hydrogen was created or how it survived the extreme UV radiation and what is its primary excitation mechanism (Akras et al., 2020).

The Low ionisation structures are further separated in two categories, depending on their velocities. So, there are the Slow Low Ionisation Structures, or SLOWERS with velocities between 30 km/s and 100 km/s and the Fast Low Ionisation Structures or FLIERS with velocities from 24 km/s to 200 km/s (Gonçalves et al., 2009). Depending on their morphology

and their kinematics, Gonçalves et al. (2001) classified these structures as knots, filaments, jets and jet-like systems. Each one of these classes can be found in axisymmetric pairs or isolated. Jets seems to be linked to the existence of an interactive binary system. If this is the case, an accretion disk can be formed, causing the collimation of the jets. As for the knots, their formation mechanism probably depends on whether they appear in pairs or alone. Some theoretical scenarios support the idea that pairs of knots were created by jets which no longer exist or are unobservable.

LISs can be present in every morphological class of planetary nebulae, which may imply that they aren't connected to the mechanisms that cause the different types of morphologies in PNe (Gonçalves et al., 2001). The ISW model and the formation of jets and their interaction with the circumstellar medium are some of the most common models for the formation of LISs. Another proposed mechanism for their formation is the Rayleigh-Taylor instability, which is a hydrodynamic instability caused in gas layers with different densities. When these layers mixed, the chemical composition and the observed structures of PNe can be affected. In this model, the interaction between the shells of a planetary nebula and the interstellar medium may result in the formation of LISs. Nevertheless, until now a general mechanism that can explain the formation of different LISs, doesn't exist.

3.4. Separation between different emission nebula

HII regions, supernova remnants, and symbiotic stars share certain characteristics with planetary nebulae, making the distinction between these objects very important. Spectroscopy plays a significant role in identifying planetary nebulae, but their distinct morphology also aids in their identification. For example, although the symbiotic stars have several similarities with planetary nebulae, they stand out because they show TiO, VO and CN absorption bands, and they are characterised by strong He II 4686 Å and Hα lines. At the same time, OVI Raman-scattered lines centred at 6830 Å and 7088 Å are observed in symbiotic stars' spectrum (Akras et al., 2019).

Also, sometimes it is difficult to distinguish HII regions from planetary nebulae. The optical spectrum of these two nebulae consists of emission lines, like the Balmer lines or the forbidden lines of Oxygen and Nitrogen. Nevertheless, the stars of HII regions are cooler than the central stars of

planetary nebulae, resulting in lower ionisation nebulae. For this reason, the spectrum of a PN contains ions of higher degree of ionisation. Additionally, they also have observational differences related to their sizes or their morphology. PNe have typical size of 1 light year, while the diameter of HII regions is about 30 light-years.

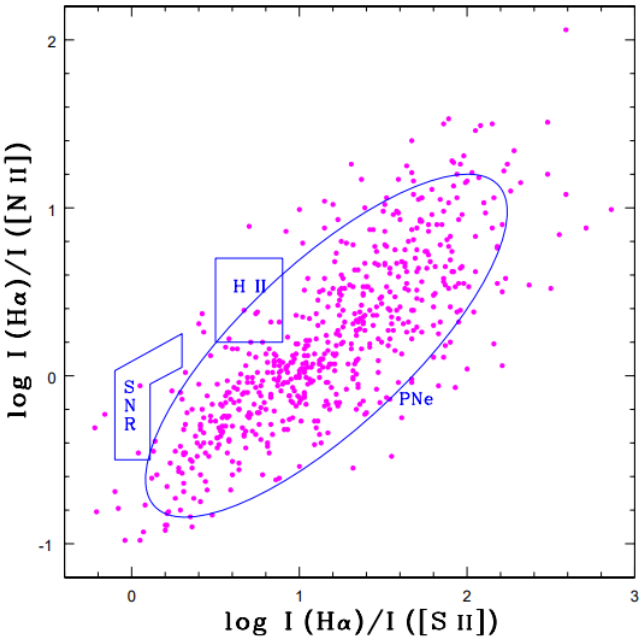

Figure 1.6: Diagnostic diagram made by the ratios $log\left(\frac{Ha}{N\,II}\right)$ and $log\left(\frac{Ha}{S\,II}\right)$ for a sample of 613 planetary nebulae (López and Riesgo, 2006)

On top of that, the diagnostic diagrams, are one of the most widely used tools to the identification of the different classes of ionised gaseous nebulae. These are plots that compare the relative line intensities of emission line ratios such as $log\left(\frac{Ha}{N\,II}\right)$ and $log\left(\frac{Ha}{S\,II}\right)$ observed in planetary nebulae, HII regions and supernova remnants, see Figure 1.6. Each object yields unique values for these ratios, leading to their placement in distinct regions on the diagnostic diagrams. This happens due to the different physical processes operating in them. For instance, the supernova remnants are mainly shock excited, which leads to lower values of the ratios. On the other hand, PNe are mostly photoionised, but it is also possible to display collimated outflows and shocks. This behaviour may influence their position on the diagnostic diagrams (López and Riesgo, 2006).

3.5. Extinction coefficient

The radiation from a planetary nebula travels through gas and dust to finally reach the observers. During this trip, the intensity of each emission line is affected by the interaction with the interstellar medium, so these lines must be corrected for the so-called interstellar extinction. The amount of extinction is usually determined by the comparison of the observed HI recombination line ratios with their theoretical values. More specifically, according to quantum mechanics, the expected ratio of Hα/Hβ emission lines is 2.86. However, due to the mentioned phenomenon, we never observe this exact value in practice. It is important to mention that this theoretical ratio is calculated for specific values of electron temperature and electron density (Ueta and Otsuka, 2021). So, conventionally to calculate the extinction we use $T_e = 10,000\,K$ and $N_e = 1,000\,cm^{-3}$.

The extinction coefficient, c(Hβ), quantifies this difference, and it is calculated via the relation:

$$c(H\beta) = \frac{1}{0.348} log \frac{F(H\alpha)/F(H\beta)}{2.86} \tag{1.4}$$

The interstellar extinction law that is used is $Rv = 3.1$ by Fitzpatrick (1999). In Equation 1.4, the number 0.348 is the relative logarithmic extinction coefficient for Hβ/Hα. After applying this correction to the line intensities, all the physical parameters of planetary nebulae are calculated, such as the electron temperature, electron density and the ionic and total abundances. More specific, the intensity is corrected for the interstellar extinction via the relation:

$$I(\lambda) = I_0(\lambda)\, 10^{-c(\lambda)}, \tag{1.5}$$

where c(λ) describes the extinction at a specific wavelength, while $I_0(\lambda)$ and I(λ) represent the reduction of the instinct flux and the observed flux, respectively. The next step is to define the observed flux at a specific wavelength λ relative to Hβ flux.

$$\frac{I(\lambda)}{I(H\beta)} = \frac{I_0(\lambda)10^{-c(\lambda)}}{I_0(H\beta)10^{-c(H\beta)}} \tag{1.6}$$

Solving the equation 1.6 for c(λ) we can find c(λ) as a function of c(Hβ).

$$\begin{aligned} c(\lambda) &= -log\left(\frac{I(\lambda/I(H\beta)}{I_0(\lambda)/I_0(H\beta}\right) + c(H\beta) \\ &= c(H\beta)\left(\frac{A_\lambda - A_{H\beta}}{A_{H\beta}} + 1\right) \\ &= c(H\beta)\left(\frac{A_\lambda}{A_{H\beta}}\right) \\ &\approx c(H\beta)\left\langle\frac{A_\lambda}{A_v}\right\rangle / \left\langle\frac{A_{H\beta}}{A_v}\right\rangle, \end{aligned} \tag{1.7}$$

where $\left\langle\frac{A_\lambda}{A_v}\right\rangle$ and $\left\langle\frac{A_{H\beta}}{A_v}\right\rangle$ represent the relative extinction at a wavelength λ and at Hβ, respectively, relative to V. Both of these ratios are provided by the extinction law. So, if Equation 1.7 is substituted in Equation 1.5, the corrected intensity is finally calculated.

3.6. Electron temperature and electron density from emission lines

The electron temperature in PNe is calculated directly by intensity ratios of some typical emission lines. Commonly, the ions of [N II] and [O III] are used for the calculation of the electron temperature. These ions produce emission lines in different upper levels with different excitation energies in the optical range of the electromagnetic spectrum. The relative strength of these lines has an impact in the electron temperature. Figure 1.7 shows the energy-level diagrams of [N II] and [O III]. For my analysis, I used the electron temperature resulting from the emission lines of single ionised Nitrogen and double ionised Sulphur. The temperature from [O III] cannot be calculated in our analysis because the line [O III] 4363Å isn't calculated in our data. The exact relations that give these temperatures are:

$$[N\,II]\frac{\lambda6548 + \lambda6583}{\lambda5755} = \frac{8.23exp\,(2.50 \cdot 10^4/T)}{1 + 4.4 \cdot 10^{-3}\,n_e/\sqrt{T}} \tag{1.8}$$

$$[S\,III]\frac{\lambda9532 + \lambda9069}{\lambda6312} = \frac{5.44exp\,(2.28 \cdot 10^4/T)}{1 + 3.5 \cdot 10^{-4}\,n_e/\sqrt{T}} \tag{1.9}$$

The first one is more representative for the low ionisation regions in addition to the second one which is more representative for the high

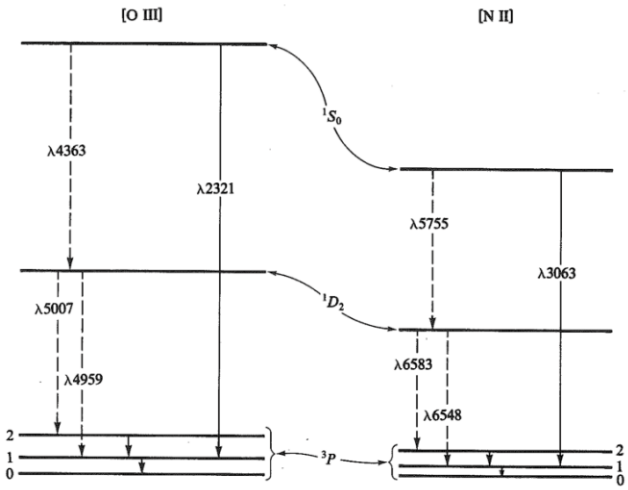

Figure 1.7: The energy-level diagram for [N II] and [O III] from Osterbrock, Astrophysics of Gaseous Nebulae and Active Galactic Nuclei. The dashed lines represent the emission lines in the optical region, while the emission lines in infrared and ultraviolet are indicated by solid lines.

ionisation regions of the nebula. Most of PNe are so highly ionised that the lines of [N II] are relatively weak. So, considering the different excitation energies at each region of the nebula, each ion refers to a specific area and not to the whole nebula. In this study, Equation 1.8 is used for the outer structures of the nebula, where structures with lower ionisation level are observed. Additionally, for the inner parts of the nebula, Equation 1.9 is used.

On the other hand, the electron density is calculated via the ratios of emission lines of the same ion emitted from different upper states but with approximately the same excitation energy. The most common lines for this calculation are the emission lines of [O II], [S II], [Cl III] and [Ar IV]. Figure 1.8 displays the energy-level diagrams for the ions [O II] and [S II]. The electron density in PNe turns out to be almost the same, either we use the single ionised Sulphur or the single ionised Oxygen.

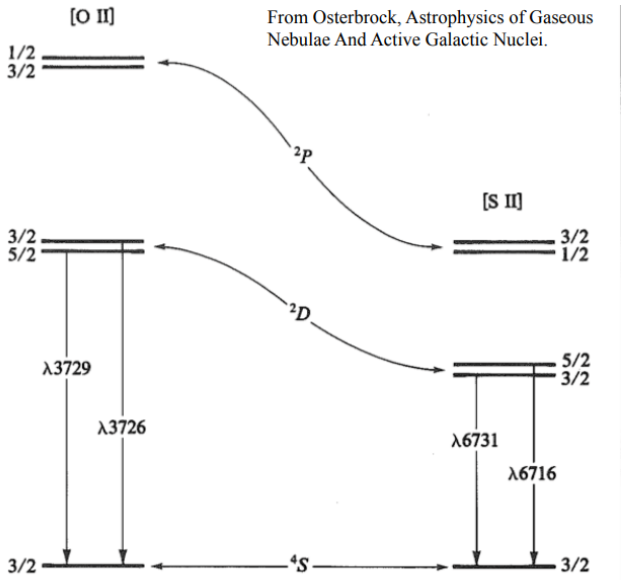

Figure 1.8: The energy-level diagram for [S II] and [O II] from Osterbrock, Astrophysics of Gaseous Nebulae and Active Galactic Nuclei

3.7. Abundances of planetary nebulae

During the evolutionary stages of the progenitor star, He and significant amounts of C and N are produced by nucleosynthesis. Throughout the AGB phase strong stellar winds occur and the elements ejected from the stellar surface enrich the planetary nebula, that is now formed, as well as the interstellar medium. Lastly, in order to investigate stellar evolution, nucleosynthesis as well as the chemical evolution of galaxies, it is crucial to accurately determine the chemical abundances in PNe.

The first step to calculate the abundances in PNe is the determination of electron temperature and electron density. Then, the ionic abundances can be calculated either from their emission lines or by photoionised models. More specifically, the ionic abundances can be derived from the analysis of Collisionally Excited Line (CEL) or Optical Recombination Line (ORL) spectra, by empirical relations, or by applying photoionisation models, or by a combination of both methods. The use of ORL is required for some elements (such as He) and ions (such as N++ if only the optical spectrum is available), while the use of CELs may be inevitable for others. However, ORL aren't always detectable, and this is why it is preferable to use CEL to calculate abundances (Goncalves et al., 2006). So, the chemical composition of a planetary nebula is generally determined from

the forbidden lines. These lines seem to be more representative for regions with high temperatures, while the recombination lines are mainly referred to regions with low temperatures. At this point, it is worth mentioning that, there are differences in the chemical composition between different planetary nebulae. For instance, some are rich in Carbon with almost two times more Carbon than Oxygen, while others are overabundant in Nitrogen.

When determining the ionic abundances, the total elemental abundances are calculated by simply adding the ionic abundances of the same ion together. Nevertheless, it is important to note that some ions of certain elements may be unobservable in the visible spectrum, leading to inaccuracies in the calculation of total abundances. For instance, in the case of Nitrogen, in the optical range of the electromagnetic spectrum we can observe only the single ionised Nitrogen and not all the other ions. Fortunately, the use of the Ionisation Correction Factors (ICFs) can improve the problematic situation, but it cannot solve it. The relation that gives the ICFs is empirical and uses a certain value for the electron density ($n_e = 1,000\, cm^{-3}$) and electron temperature ($T_e = 10,000\, K$). Alexander and Balick (1997) using the above method, showed that the error in the calculation of the abundance of He, O and N is less than 5% and for Ne, S and Ar is less than 25%. The ratios between various elements, such as N/O, S/O, N/S, and He/O, have also been studied. These ratios provide information about the evolution and origin of PNe, their progenitors and the whole Galaxy.

Another problem that usually arises is that the calculated abundances from ORL disagree with those determined from CEL (García-Rojas et al., 2021). Specifically, the first method gives significantly higher values in comparison with the second method (Torres-Peimbert, 2015). The ratio of these different calculations is called Abundance Discrepancy Factor (ADF). For most of PNe, the ADF usually takes small values between 2 and 3 (García-Rojas et al., 2021). The ADF still remains an open question in the field of PNe.

Chapter 2

The Planetary Nebula NGC 3242

The planetary nebula NGC 3242, also known as The Ghost of Jupiter, is located approximately $1,279^{+63}_{-62}$ pc away (Bailer-Jones et al., 2021), in the constellation of Hydra, and has an apparent magnitude of 8.6. The central star of the planetary nebula is a white dwarf with temperature about 80,000 K and a radius $R \approx 0.14 R_{\odot}$ (Pottasch and Bernard-Salas, 2008). As for its morphology, it is a multiple shell PN (Monteiro et al., 2013). More specific, it has an inner elliptical shell with dimensions of $28''x20''$, which is surrounded by an external almost elliptical envelope of $46''x40''$ (Gómez-Muñoz et al., 2015). The inner elliptical shell, also, contains an inner bright rim, resulting from interactions with the stellar wind (Phillips et al., 2009). A pair of knots oriented along the major axis (NW-SE) are also part of the inner shell. Gómez-Muñoz et al. (2015) proposed the idea that a shock front created by the interactions of stellar winds led to the formation of the inner shell, while the knots were probably formed by a later ejection, and they were the last morphological structures formed in NGC 3242 (Gómez-Muñoz et al., 2015).

In addition, deep images have revealed a massive halo surrounding the two shells, which seems to be the relic of the AGB envelope (Corradi et al., 2003). Also, at least three rings and two arc-like features are observed within this halo, which were probably created at the end of the AGB phase (Gómez-Muñoz et al., 2015). Lastly, the nebular core is shown to have a cylindrical structure (Meaburn et al., 2000). According to previous studies, all the different morphological structures may come from

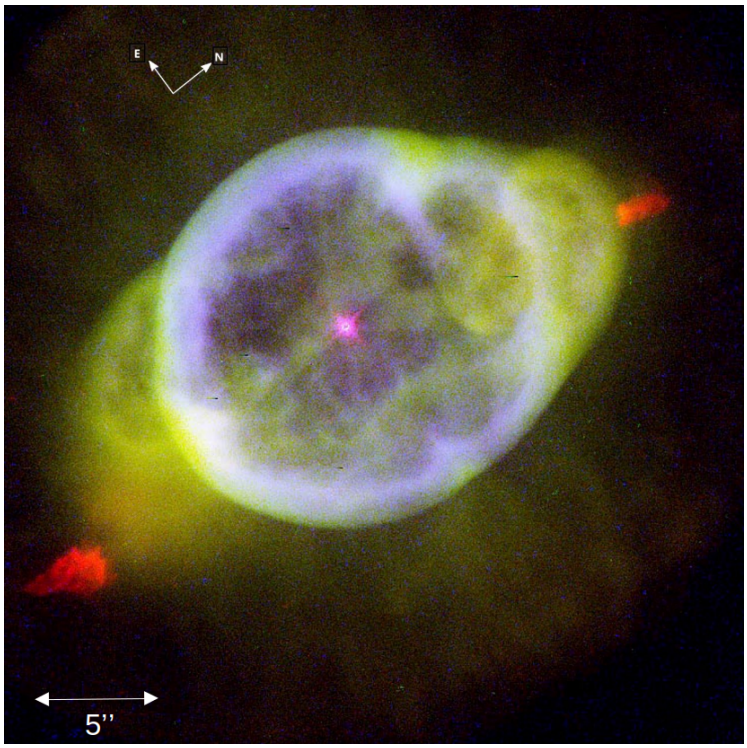

Figure 2.1: NGC 3242 image from Hubble Space Telescope. The presence of two knots (the red structures) on both poles of the planetary nebula is clear. Colours and filters: O I 631 nm, N II 658 nm, S II 673 nm (Bruce Balick and Jason Alexander (University of Washington), Arsen Hajian (U.S. Naval Observatory), Yervant Terzian (Cornell University), Mario Perinotto (University of Florence), Patrizio Patriarchi (Arcetri Observatory) and NASA/ESA)

different episodes of mass loss during the AGB phase of the progenitor star, (Barria and Kimeswenger, 2018) while all of them were made in a clumpy environment (Gómez-Muñoz et al., 2015).

One of the biggest enigma around NGC 3242 is connected to the existence of LISs, in Figure 2.1 LISs are presented with red colour. In general, several authors have investigated how the physical properties of PNe change at the positions of LISs e.g (Hajian et al., 1997; Balick et al., 1998; Gonçalves et al., 2001; Akras and Gonçalves, 2016; Akras et al., 2020; Akras et al., 2022). According to these studies, the electron temperature seems to remain almost constant throughout the nebula. On the other hand, the electron density is found to be systematically lower at the LISs, which is in conflict with the theoretical scenarios about the formation of LISs. Furthermore, there is no variation in the elemental

abundances of Oxygen and Helium from region to region, but this isn't the case for the Nitrogen and Sulphur for which an overabundance was found at the LISs (Monteiro et al., 2013). Nevertheless, as it was mentioned in section 3.7 for Nitrogen ICF is typically very high, resulting to less representative value for its abundance (Monteiro et al., 2013).

For the extinction coefficient, determined from the Balmer ratios, there are slightly different results according to different authors. More specific, c(Hβ) ranging from 0.05 to 0.2 (Monreal-Ibero et al., 2005; Pottasch and Bernard-Salas, 2008; Miller et al., 2016). The electron temperature from previous studies is $T_e \approx 11,500\,K$ calculated either from [O III] or from [N II] (Krabbe and Copetti, 2006; Pottasch and Bernard-Salas, 2008; Monteiro et al., 2013). As for the electron density, it is about $2,500\,cm^{-3}$ with slight differences depending on the emission lines that are used in every case (Pottasch and Bernard-Salas, 2008). Lastly, the logarithmic total flux of Hβ, in $ergs\,cm^{-2}\,s^{-1}$, is -10.45 (Tsamis et al., 2003).

As for the kinematics of NGC 3242, the inner and the outer shells have expansion velocities of $23 \pm 1\,km/s$ and $13 \pm 1\,km/s$, respectively (Gómez-Muñoz et al., 2015). In the contrary, LISs have much higher velocities than the surrounding nebula, which may indicate that they are connected to jets (Gómez-Muñoz et al., 2015). These velocities are about $117\,km/s$ and $140\,km/s$ (Gómez-Muñoz et al., 2015).

Chapter 3

Spectroscopic analysis of NGC 3242

For the primary spectroscopic analysis of NGC 3242, optical 3D data from Multi Unit Spectroscopic Explorer at VLT were used. All the physical parameters of the PN were calculated with these data. In addition, infrared image data from Spitzer Space telescope (SST), were employed for a multiwavelegth study.

1. Multi Unit Spectroscopic Explorer

Multi Unit Spectroscopic Explorer (MUSE) at VLT, is an Integral Field Unit (IFU) operating in the visible range of the electromagnetic spectrum (from 465 nm to 930 nm). In slit spectroscopy, a single slit is placed into the focal plane, which is then re-imaged onto the detector by the spectrograph. The drawback of this method is that only a small part of the object, is sampled at once, so it takes multiple sequential exposures with different slit positions to completely cover an item in two dimensions. With Integral Field Spectroscopy, this problem of the slit spectroscopy is now solved. IFU produce data in 3 dimensions, two spatial directions and one spectral directions, (Figure 3.1). More specific, the signal from each pixel is fed into a spectrograph, which then generates a spectrum for each one of the pixels. The result of this procedure is a data-cube which contains the entire 2D field of view plus the third dimension created from the spectrograph, which splits the light into its different colours or

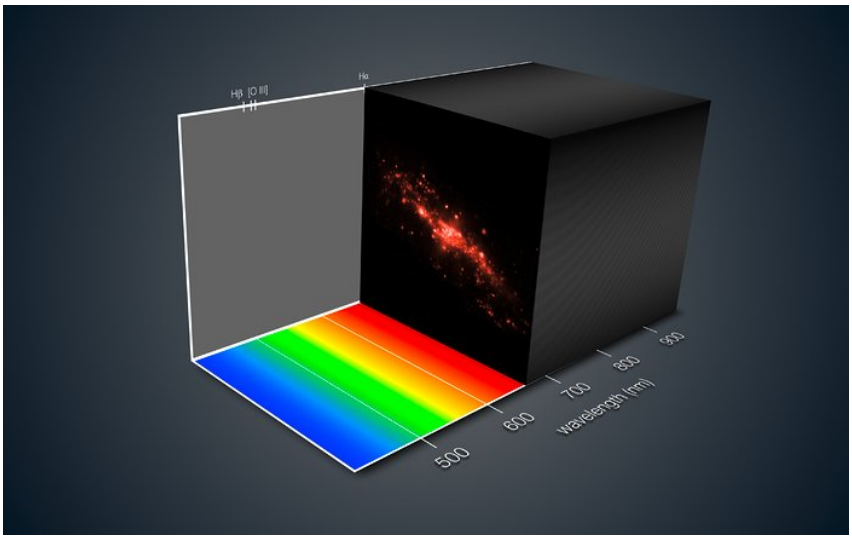

Figure 3.1: This image shows how MUSE instrument on ESO's Very Large Telescope produces data in 3D (Credit: ESO/MUSE consortium/R. Bacon/L. Calçada)

wavelengths (Bacon et al., 2010).

With data-cubes, it's easier to study the spatial distribution of the object's physical properties, such as the temperature the density or the chemical composition, and how these properties vary across the object. IFS has been used to study a wide variety of astronomical objects, from galaxies and nebulae to stars and exoplanets (Allington-Smith, 2006). IFS has also been used to study the inner workings of active galactic nuclei and to search for signs of life in the atmospheres of exoplanets (Allington-Smith, 2006).

With IFS, astronomers can study the spectra of individual regions within an object, such as the regions surrounding a black hole or the regions where stars are forming within a galaxy. This level of detail can provide valuable insights into the physical processes that contributed to the creation of the object and its ongoing evolution over time. IFS has become an important tool for modern astronomy and is expected to play a major role in our understanding of the universe in the years to come. In the case of planetary nebulae, IFS makes easier the spatial analysis of PNe's physical and kinematic properties, which is very important for understanding the morphological characteristics within the different ionisation layers (Danehkar, 2022).

1.1. Extraction of emission line maps

The first step in my master thesis was to extract the emission maps of some optical emission lines, typically observed in PNe. A python script was used for this analysis. By this code, the user can choose the desired line and a number of lines before and after the main line that the code will use to make a Gaussian fit (see Figure 3.2). At the same time, the continuum is subtracted, so the user can have a "clean" emission line map without the contribution of the continuum radiation. This procedure was repeated for every optical emission line that was detected by the MUSE instrument.

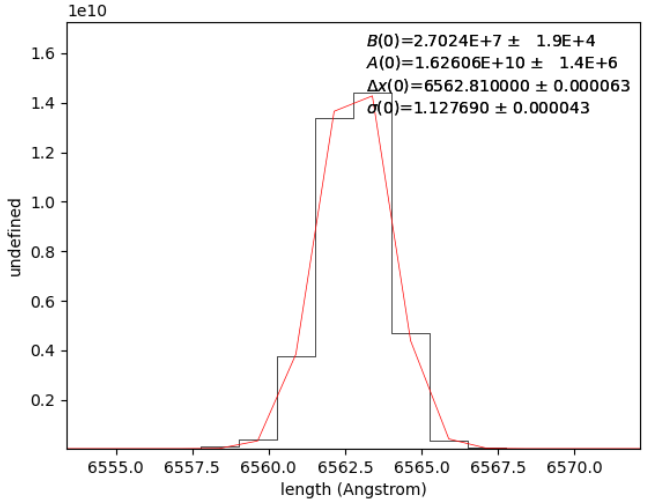

Figure 3.2: The Gaussian fit for the emission line Hα as extracted from the MUSE data-cube

For the analysis of NGC 3242, two data-cubes were available with two different exposure times. The first one had exposure time equal to 814s and the second one was the short exposure data-cube with exposure time 10s. At the beginning the long exposure data-cube was used for every line, but the Balmer recombination lines and the [O III] lines, which are very bright, were saturated. So, in order to solve this problem, for the lines [O III] 4959 Å, 5007 Å, Hα and Hβ, the short exposure data-cube was used. For instance, Figure 3.3 shows the emission line map of Ha extracted both from the short and long exposure data-cube. The remaining lines were extracted from the long exposure data-cube in order to achieve higher s/n ratio.

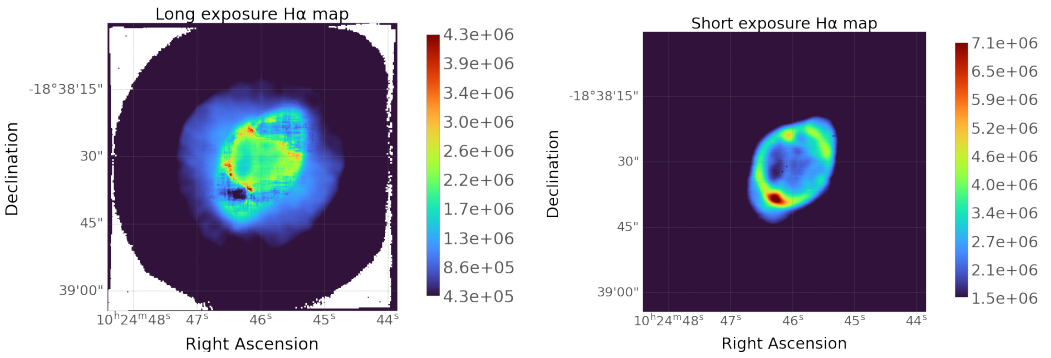

Figure 3.3: Left panel: Saturated Ha map extracted from the long-exposure data-cube. Right panel: The Ha emission line map extracted from the short-exposure data-cube

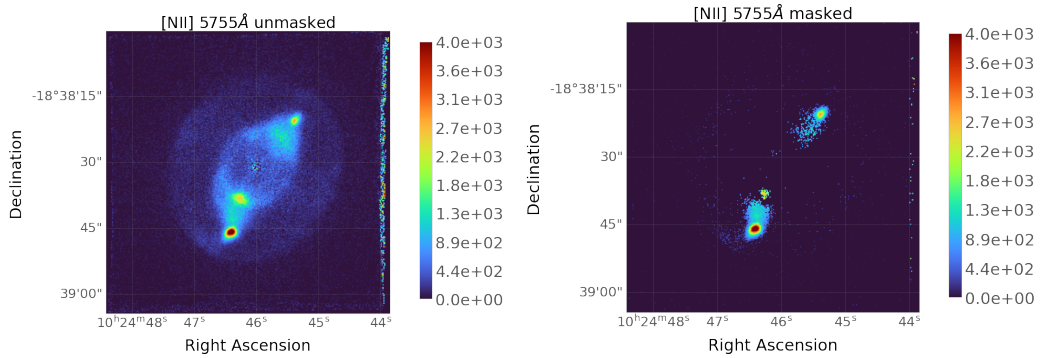

Figure 3.4: Left panel: The map of the emission line [N II] 5755 Åwithout mask. Right panel: The map of the emission line [N II] 5755 Åwith mask

Lastly, as it was mentioned before the lines [N II] 5755 Å, 6548 Å and 6584 Å are very important in the calculation of the ionic temperature. The problem here is that the first of these three lines is too faint to be clearly observed. More specific, the line [N II] 5755 Å is very noisy in every structure of NGC 3242 except of the LISs. This means that the emission has low S/N, i.e. the emission line is comparable with the background radiation. As a result of the poor emission of the line, the calculated electron temperature from Nitrogen is representative only at the position of the LISs. For this reason, a mask was applied in every emission map to chase away the areas that the emission lines are very faint and cause problems to the results. This mask replaces every pixel value that doesn't satisfy the criteria below with zero. For instance, Figures 3.4 displays the

[N II] 5755 Å line map before and after applying the mask.

- emission map / error map ≥ 5
- emission map > 0.01 Hβ map
  (or > 0.005 in the case of [C I] 8727 Å)

2. SATELLITE

The next step in my thesis was to use these extracted maps to perform a spectroscopic analysis of the planetary nebula NGC 3242, via the python code SATELLITE, which is developed by Akras et al. (2022). This code can be used for spectroscopic characterisation of extended nebulae like planetary nebulae, galaxies or HII regions. The code contains 35 emission lines typically observed in ionised nebulae (Table 3.1) and it can do both 1D and 2D analysis. In the first case, a number of pseudo-slits is used for the simulation of slit spectroscopy that was commonly used before the IFU era.

The code takes the maps from the available emission lines as an input and computes all the nebular physical parameters with their uncertainties. More specifically, as an output the code produce some ASCII files with the computed electron temperature, electron density, extinction coefficient, ionic and total abundances, ICFs, line intensities and some line ratios. For handling uncertainties, a Monte Carlo approach is employed, allowing the user to select the desired number of Monte Carlo counts. SATELLITE code has four modules, and every physical parameter can be calculated for each one of these modules. At the same time, the SATELLITE produces some important plots depending on the module that the user choose. All the outputs of each module are saved in different files. Below, we analyse in more detail the modules which are available in SATELLITE.

- specific slit analysis

This module offers the opportunity to study specific morphological structures of the nebula. The user can place ten pseudo-slits on regions of choice on the nebula. The dimensions (in pixels) and the position angle of the slits are free parameters too. Figure 3.5 shows ten pseudo-slits placed on the [N II] 6584 Å map of NGC 3242.

Line	wavelength(Å)	Line	wavelength(Å)
Hα	6563	[O II]	7330
Hβ	4861	[O I]	6300
H I	4340	[O I]	6363
He I	5876	[S II]	6716
He I	6678	[S II]	6731
He II	5412	[S III]	6312
He II	4686	[S III]	9069
[N II]	5755	[Cl III]	5517
[N II]	6548	[Cl III]	5538
[N II]	6583	[Ar III]	7136
[N I]	5199	[Ar IIII]	4712
[O III]	4959	[Ar IIII]	4740
[O III]	5007	[C I]	8727
[O II]	3727	[C II]	6461
[O II]	3729	Ne III	3868
Ne III	3967		

Table 3.1: The emission lines that are available in SATELLITE code for Spectroscopic analysis of nebulae.

- radial analysis

The radial analysis task uses a pseudo-slit which begins from the centre of the nebula and extends to the outer parts. By this analysis, the user can test how the physical parameters of the nebula change with the distance from the central star, in the case of PNe, or from the central part of another nebula like HII regions. The position angle, the width and the length of the slit are provided by the user. The code, also, produces the radial profiles of all the emission lines that are selected by the user. Only the values of pixels that satisfy the F(Hα)>0, F(Hβ)>0 and/or F(Hα)>2.86 F(Hβ) are summed up.

- angular analysis

By using this module, the users can investigate how the physical parameters of the nebula change with the angle of the pseudo-slit. In the angular analysis, a series of pseudo-slits are employed, positioned radially at various angles ranging from 0 to 360 degrees (Figure 3.6). The step size

between each angle is a free parameter that can be adjusted according to the specific requirements of the analysis. Every slit begins from the centre of the nebula to the outer parts. Except of the angle step, the user can choose the minimum and the maximum position angle, the width and the length of the pseudo-slits. The code then integrate the values for every one of the pixels that are inside the region that the slit covers. Nevertheless, there are some restrictions defined by the relations F(Hα)>0, F(Hβ)>0 and/or F(Hα)>2.86 F(Hβ). If these criteria aren't satisfied at some point, then the code returns zero values.

- 2D analysis

Lastly, via the 2D analysis module, SATELLITE performs spectroscopic analysis in two spatial dimensions at the same time. The code produces not only 2D maps for every physical parameter of the nebula but also the pixel distribution of each map. On top of that, SATELLITE produce diagnostic diagrams which compare the relative line intensities of some ratios observed in supernova remnants, planetary nebulae and H II regions (López and Riesgo, 2006). These nebulae are expected to occupy distinct regions on these diagrams due to the different excitation mechanisms of each one of them. Lastly, there are some restrictions in this case too. If these criteria F(Hα)>0, F(Hβ)>0 and/or F(Hα)>2.86 F(Hβ) aren't satisfied, then the code returns zero values.

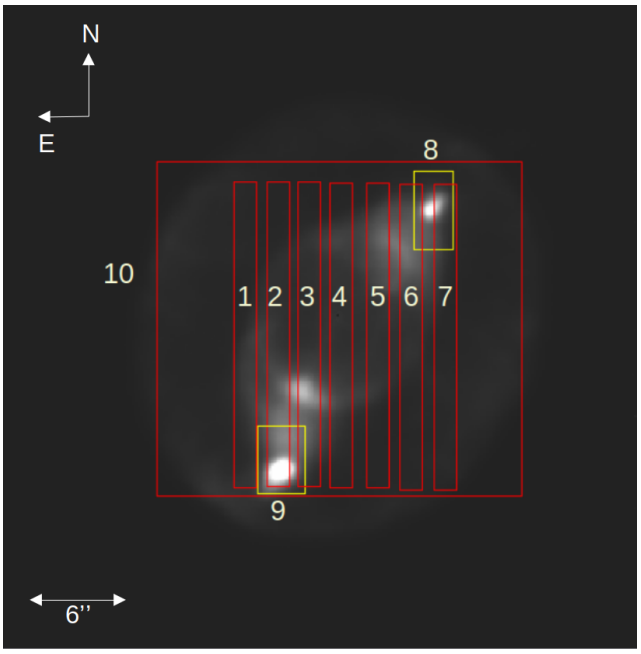

Figure 3.5: This figure shows an example of ten pseudo-slits placed on the [N II] 6584 Åemission map

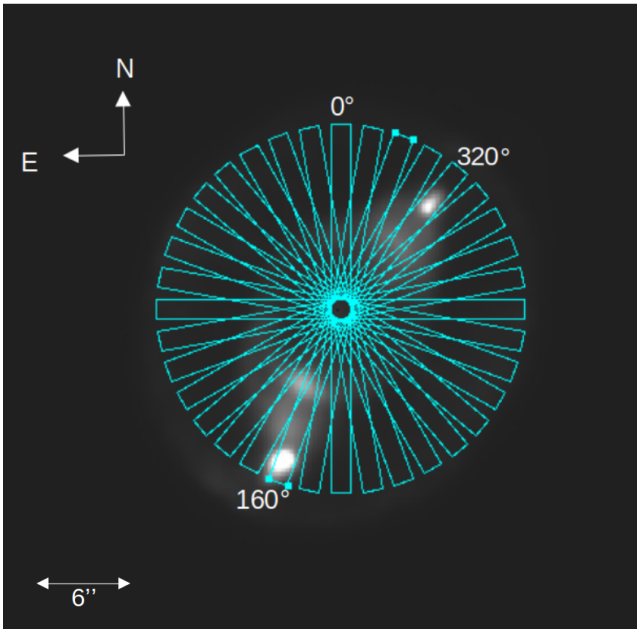

Figure 3.6: This figure shows ten pseudo-slits placed from 0 o 360 degrees with a step of 10 degrees ([N II] 6584 Å emission map). The angles 160 and 320 degrees, where the LISs are found, are marked.

3. Spitzer Space Telescope (SST)

Spitzer observed the PN NGC 3242 with the use of the Infrared Array Camera (IRAC). SST was an infrared space telescope which launched in 2003 and stopped its operations in 2020. One of the instruments that Spitzer used was IRAC, a four-channel camera that provided simultaneous 5.2' × 5.2' images at 3.6, 4.5, 5.8, and 8.0 μm. The filters had bandwidths $\Delta\lambda$ = 0.75 μm, $\Delta\lambda$ = 1.9015 μm, $\Delta\lambda$ = 1.425 μm and $\Delta\lambda$ = 2.905 μm, respectively (Phillips et al., 2010). In Figure 3.7, we can see the transition curves of IRAC's filters. With the combined results from the three out of four IRAC bands, RGB images of the PN were created. Lastly, radial profiles of the bands and their ratios were made to explore for potential trend from the inner to the outer parts of the nebula. Unfortunately, LISs were not detected in any of the images produced by IRAC.

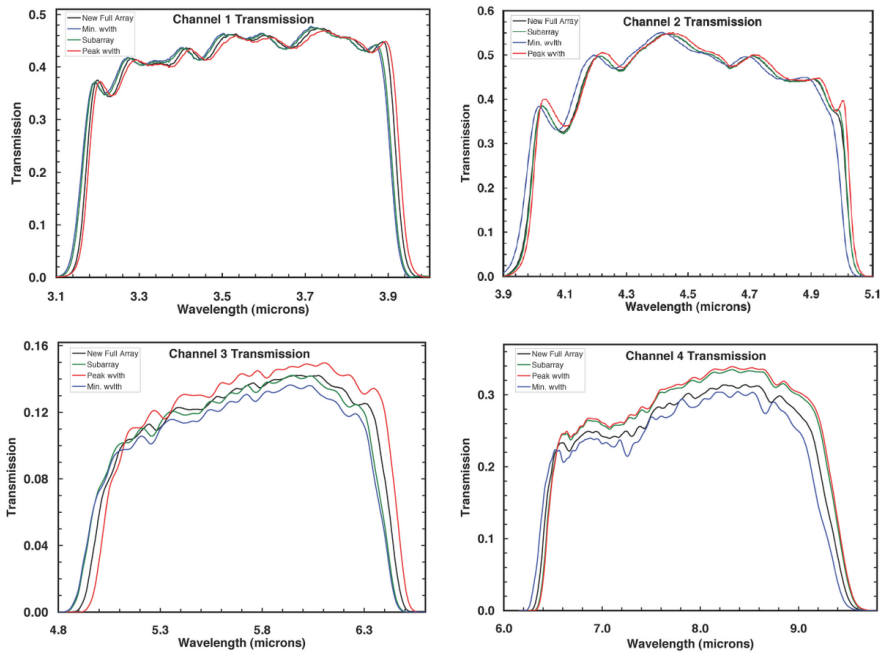

Figure 3.7: The following figures display the response curves for all 4 IRAC channels. The full array average curve is displayed in black. The sub-array average curve is in green. The extrema of the full array per-pixel transmission curves are also shown for reference, NASA/IPAC Infrared Science Archive

Chapter 4

Results and Interpretation

Following the procedure that was mentioned in the previous chapter, a thorough multiwavelegth spectroscopic analysis of NGC 3242 was made. SATELLITE's modules employed with MUSE data were used for the characterisation of the planetary nebula, having as a main goal to understand the nature of the LISs. Subsequently, the most important results are presented, divided into subsections according to the type of analysis used each time.

1. MUSE optical data

1.1. Specific slit analysis

1.1.1. Increasing width/length of the slit

Firstly, the specific slit analysis module was used in order to test how the dimensions of the slit affect the results for the physical parameters of the planetary nebula. To be more specific, ten slits were employed with width that increased gradually by ten percent of the total width of the planetary nebula. The length of the slits remained fixed throughout this analysis. By this procedure, ten slits were created with the same length but larger width. The tenth slit was the one that covered the whole nebula. The same procedure was repeated, but this time the width of the slit

was constant and the length was increasing. In Figure 4.1 we can see the position of the slits. In both cases, none of the physical parameters change significantly. In Figures 4.2 and 4.3 the electron temperature and the electron density as well as the c(Hβ) are presented respectively calculated from the analysis in which the length of the slit was gradually increasing. Te gradually decreases but not significantly, while Ne is almost constant within the errors. Lastly, c(Hβ) remains the same from one slit to another.

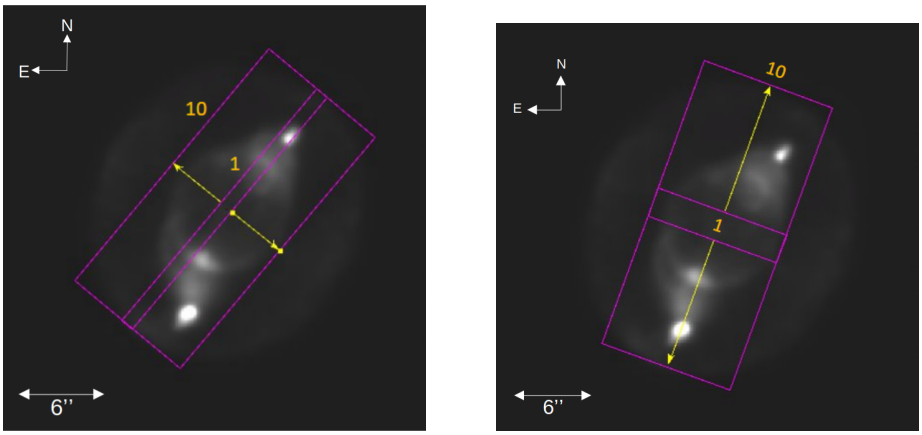

Figure 4.1: Left panel: The width of the slit increases in the direction indicated by the yellow arrows, Right panel: The length of the slit increases in the direction indicated by the yellow arrows

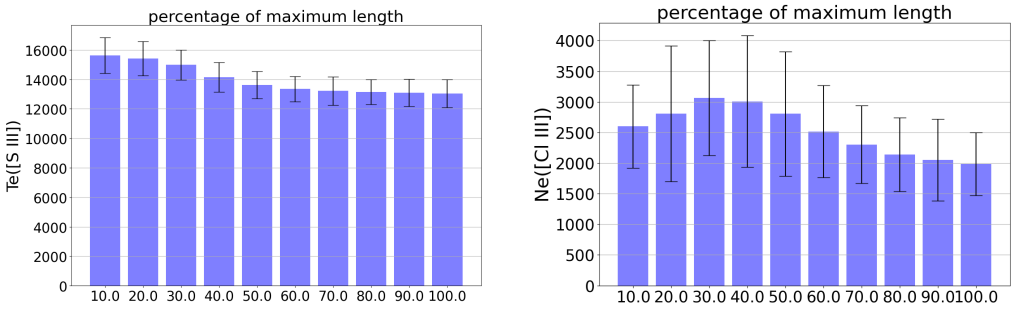

Figure 4.2: Left-panel: Te([SIII]) and Right panel: Ne([ClIII]) from the specific slit analysis with increasing length of the slit

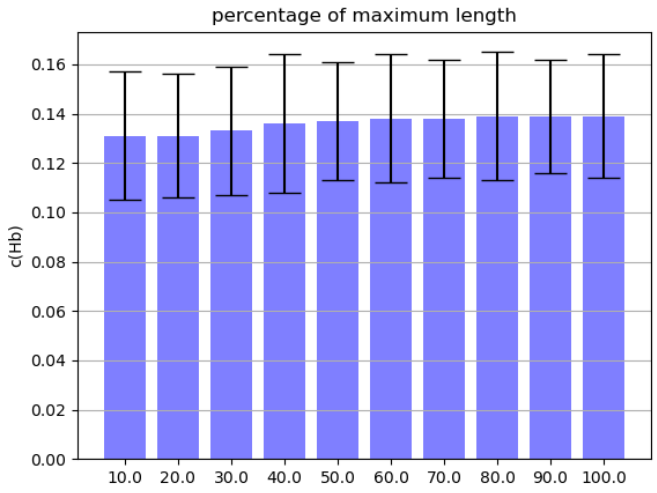

Figure 4.3: c(Hβ) from the specific slit analysis with increasing length of the slit

1.1.2. Comparison between the inner and the outer structures

This module was also used to test if the nebular parameters change significantly from the LISs to the innermost regions. In Figure 4.4 we can see the positions of the slits and in Figures 4.5, 4.6 and 4.7 some of the main results.

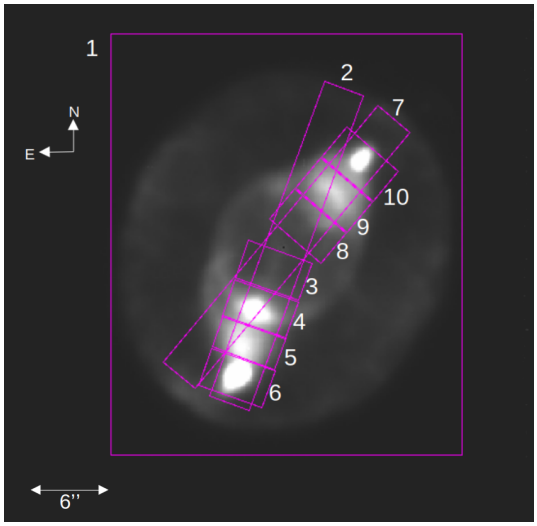

Figure 4.4: This figure shows the positions of ten slits that were used in this analysis

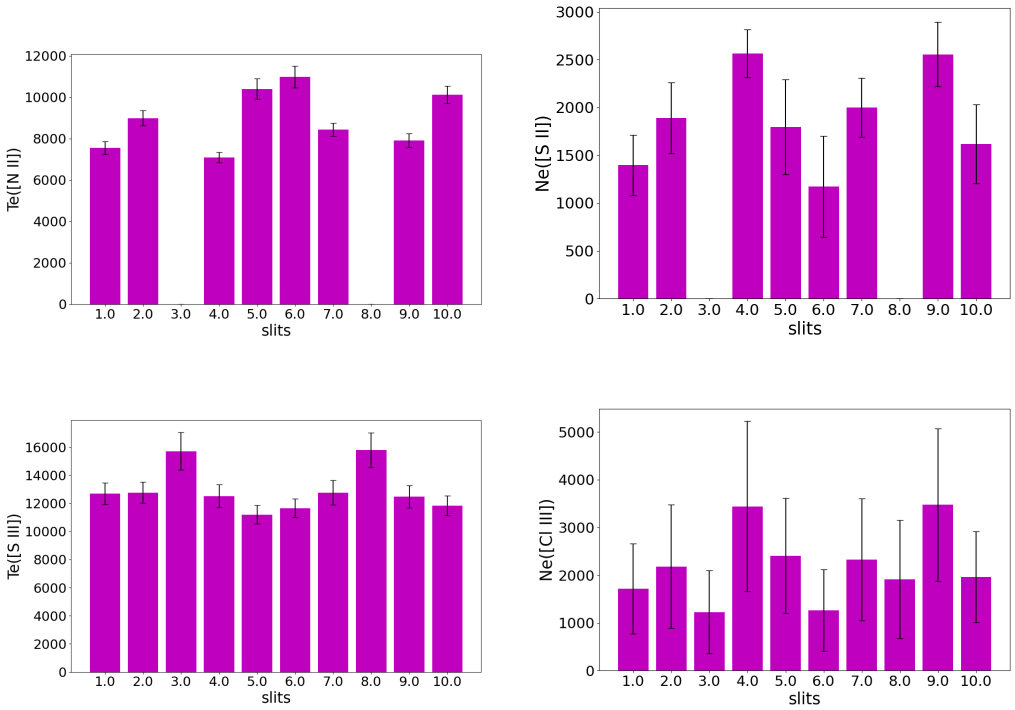

Figure 4.5: Upper-Left panel: Te[N II], Upper-Right panel: Ne[S II], Bottom-Left panel: Te[S III], Bottom-Right panel: Ne[Cl III].

Figure 4.5 displays the Te and Ne from this analysis. Firstly, Te([N II]) is calculated (upper-left panel). In slits 3 and 8 the electron temperature isn't calculated at all. Due to the application of a mask that removed all the values of [N II] 5755 Å near the centre of the nebula, the calculation of the electron temperature is limited to the (LISs) only (see the relation 1.8). As for Te([S III]) (bottom-right panel) slightly increases in slits 3 and 8 while in the other regions is almost constant. Moving to the electron density, since Te([N II]) isn't calculated at slits 3 and 8, neither Ne([S II]) is calculated at these regions. The variation is within the errors when Ne is calculated from [Cl III] (bottom-right panel).

In Figure 4.6 some ionic abundances are displayed. We can see that none of them stay constant from one region to another. However, it is important to mention that for the calculations of the ionic abundances we used either Te([S III]) or Te([N II]). The first one was used for the high

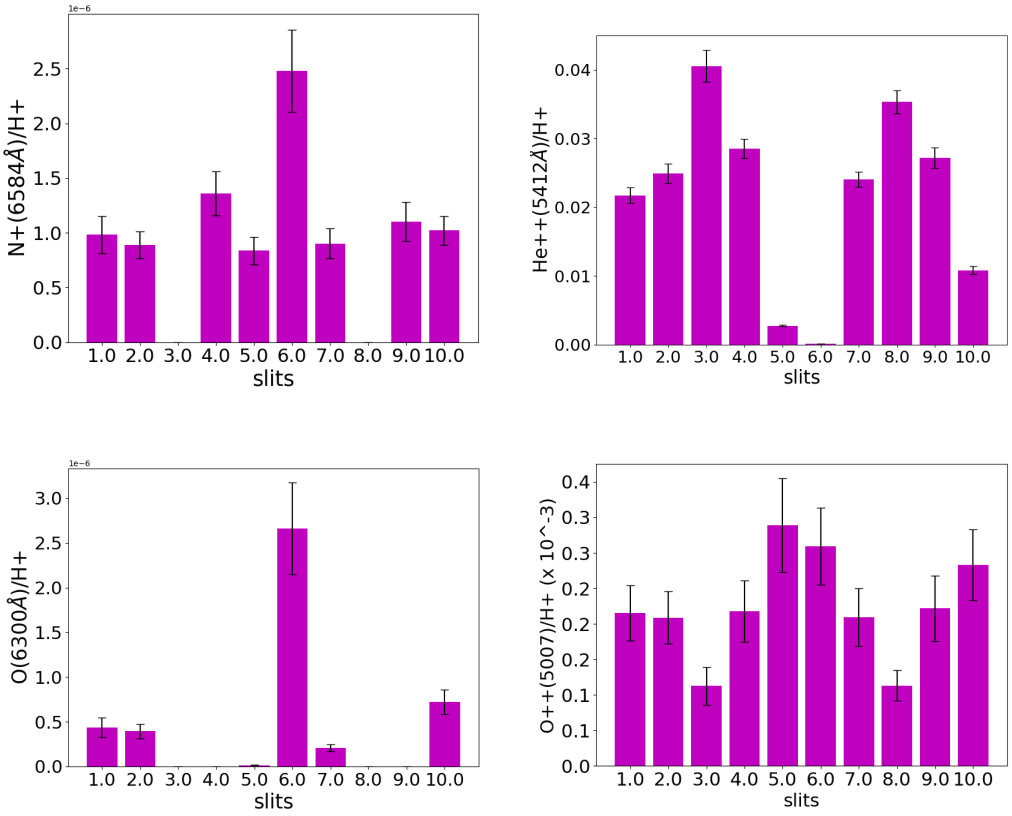

Figure 4.6: This figure shows how some ionic abundances change with the position of the slit. Upper-Left panel: abundance of [N II] 6584 Å, Upper-Right panel: abundance of He II 5412 Å, Bottom-Left panel: abundance of [O I] 6300 Å, Bottom-Right panel: abundance of [O III] 5007 Å.

ionisation ions, while the second one was used for the low ionisation ions. So, in the case of N+/H+ and O/H+ abundances, Te([N II]) was employed. At the inner nebular structures (slits 3 and 8 in upper-left panel) no N+(6584 Å)/H+ was measured. This is reasonable because Te[N II] isn't calculated in these regions and without the electron temperature nor N++(6584 Å)/H+ can be calculated. Similar behaviour is observed in O (6300)/H+ too, only now zero values are also returned by slits 4 and 9. This is probably due to the zero emission of the line [O I] 6300 Å at these regions. On the other hand, He++(5412 Å)/H+ shows significant decrease in the LISs because the emission of the line He II 5412 Å is more concentrated at the nebular centre. Afterwards, maps of the ionic

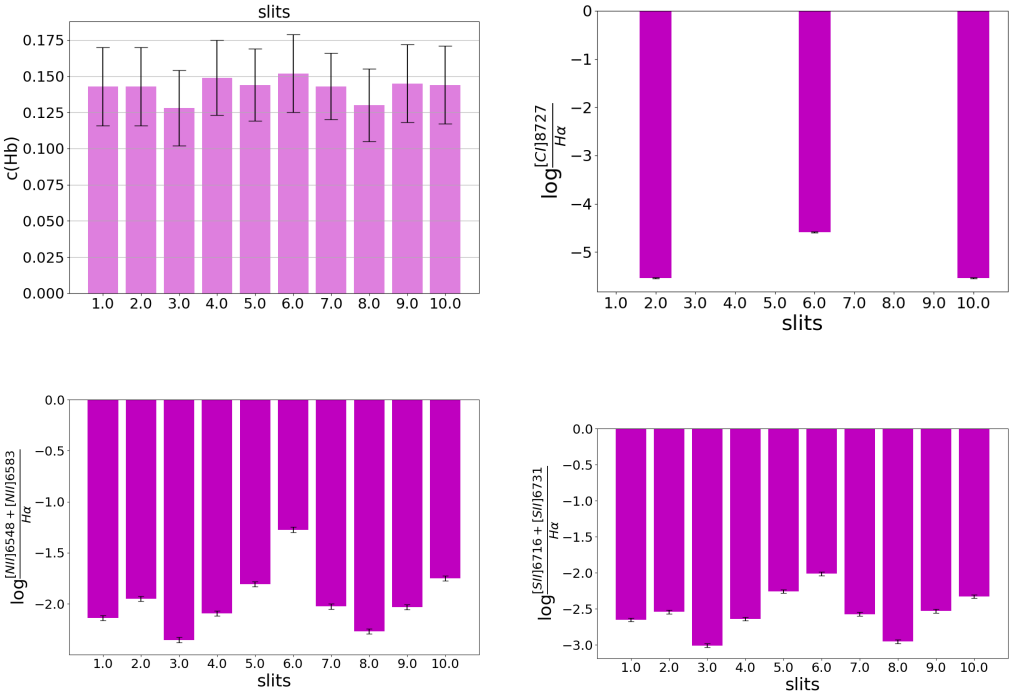

Figure 4.7: This figure shows how some emission line ratios change with the position of the slit. Upper-Left panel: extinction coefficient, Upper-Right panel: log([C I] 8727 Å/Hα), Bottom-Left panel: log([N II]/Hα), Bottom-Right panel: log([S II]/Hα).

and total abundances are presented for a more extensive and complete analysis. Lastly, the variation of O++(5007 Å)/H+ isn't so significant (bottom-right panel).

From Figure 4.7 (upper-left panel), we can see that the extinction coefficient is sufficiently constant with the position of the slit. The ratio log([C I] 8727 Å/Hα), Figure 4.7, upper-right panel, takes non-zero values only for the slits 2, 6 and 10 (see Figure 4.4). This result is the expected one because the low ionisation line [C I] 8727 Å is expected to be emitted only from the low ionisation regions. Also, at the southeast knot the emission of [C I] seems to be stronger and for this reason we notice that the emission is also detected in slit 2 which covers a bigger region and the final value is the integrated one of the whole region. Lastly, the bottom-left and bottom-right panels of Figure 4.7 represent how the ratios

log([N II]/Hα) and log([S II]/Hα), respectively, change from the LISs to the inner parts of the nebula. No significant variation was found, but we can see that at the LISs both of these ratios are larger than the surrounding nebula. This is reasonable because both [N II] and [S II] are low ionisation ions, thus we expect them to be emitted mainly from the low ionisation regions.

1.1.3. Comparison with previous studies

Ten pseudo-slits were also simulated in the same positions with Miller et al. (2016) who studied the chemical homogeneity of NGC 3242 using data from Hubble Space Telescope (HST). HST is equipped with instruments operating across the entire optical spectrum, from infrared to visible and ultraviolet. One of its instruments is the Space Telescope Imaging Spectrograph (STIS), which combines a camera with a spectrograph and operates from near-infrared to ultraviolet. Miller et al. (2016) used long slit observations and they spatially divided the main slit into nine smaller regions (see Figure 4.8). So, in our analysis, we simulated the same slits and investigated if our analysis through SATELLITE code reproduces their results.

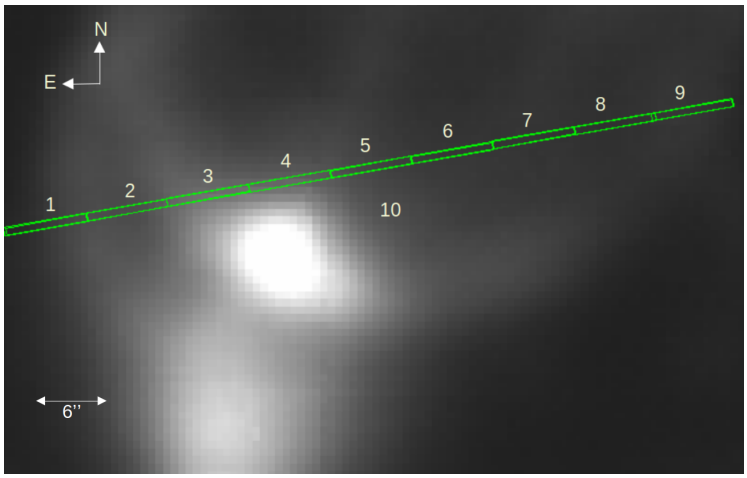

Figure 4.8: This figure shows the positions of the slits from Miller et al., 2016. In this Figure, we can see the down half part of the nebula.

In Figure 4.9 we can see that there are no significant differences between the two datasets about the intensity of the [O III] lines. On the other hand, the extinction coefficient (Figure 4.10), is systematically higher in our analysis, and the discrepancy between the two datasets is

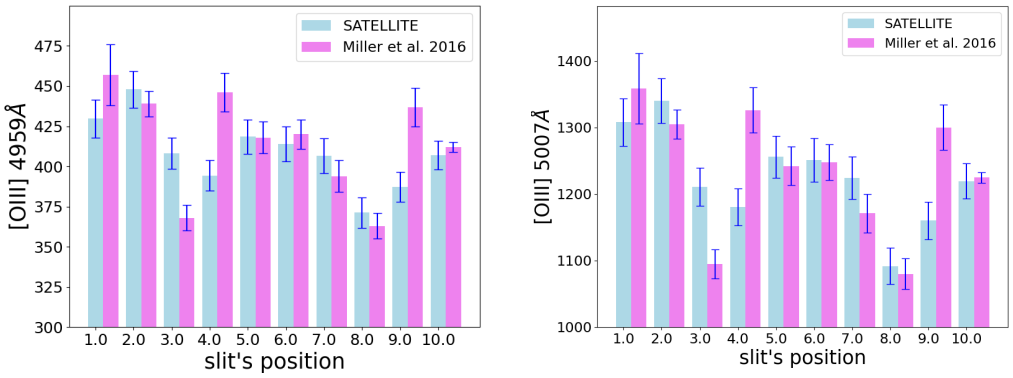

Figure 4.9: Comparison of line intensities as calculated by Miller et al. (2016) and by SATELLITE. Left-panel [O III] 4959 Å Intensity, Right-panel: [O III] 5007 Å Intensity.

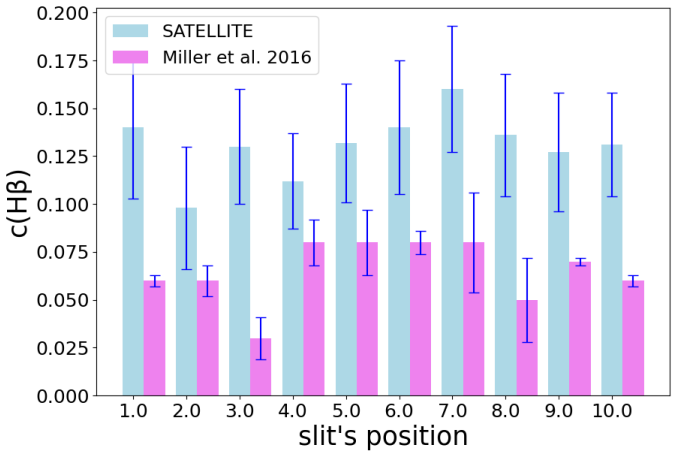

Figure 4.10: c(Hβ) from SATELLITE (light blue bars) and from Miller et al. (2016) (magenta bars).

significant. Nevertheless, our result is consistent with previous results about the extinction coefficient of NGC 3242 (Monreal-Ibero et al., 2005; Pottasch and Bernard-Salas, 2008). As for the electron temperature, Miller et al. (2016) used [O III] emission lines for its calculation. However, it should be noted that the range of MUSE data does not include all the required emission lines to calculate Te([O III]). So, instead of this, we

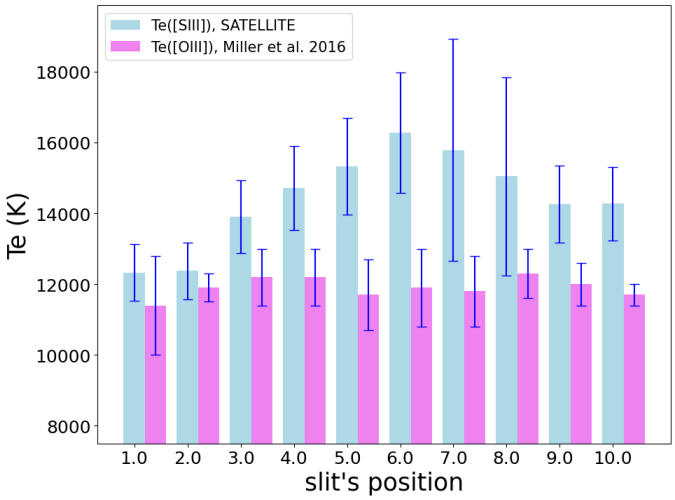

Figure 4.11: c(Hβ) from SATELLITE (light blue bars) and from Miller et al. (2016) (magenta bars).

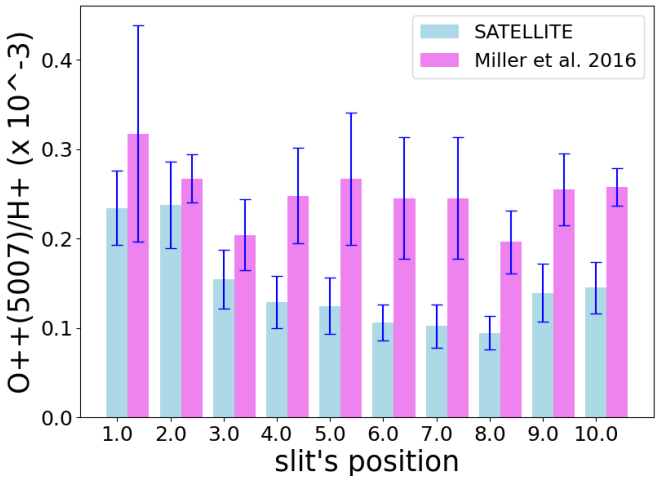

Figure 4.12: Comparison of [O III] 5007 Å abundance as calculated Miller et al. (2016) and by SATELLITE

used Te from [S III] lines (see Figure 4.11). Te([S III]) it turns out to be higher in comparison to Te([O III]). This may result in the systematic difference in O++(5007 Å)/H+ between the two datasets (Figure 4.12).

1.2. Radial analysis

This module was used to test how the nebular physical parameters change with the distance from the central star. For this purpose, two different slits were used with position angles 160 degrees and 320 degrees, where the two LISs are found. In each one of these cases the slit was extended from the central star to the outer parts of the nebula with fixed dimensions 92x10 spxales. The first LIS which is at P.A.=160^o has a distance of 13" from the central star. On the other hand, the second LIS, which is at P.A.= 320^o can be found at 16" from the central star. After the SATELLITE ran, the results were used to create the radial profiles of some typical emission lines via a python code to examine how the surface brightness of each line change with the distance from the central star.

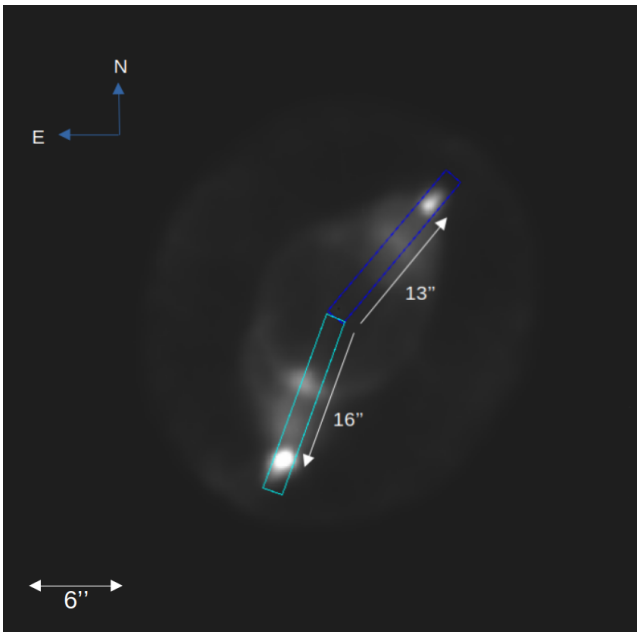

Figure 4.13: The radially placed pseudo-slits on the [N II] 6584Å emission map

Figures 4.14 and 4.15 show the results from SATELLITE for c(Hβ) (left-panel), Te[S III] and Ne[Cl III] (right-panel) for P.A. 160^o and 320^o, respectively. In both cases the extinction varies between 0.1 and 0.2 with a mean value of 0.13 which is in good agreement with previous studies, e.g. Monreal-Ibero et al. (2005). No increase of c(Hβ) at the position of the LISs was found, as it has been shown for the LISs of NGC 7009 in Akras et al. (2022). Regarding the electron temperature, it is found to be very

slit's P.A. = 160 degrees

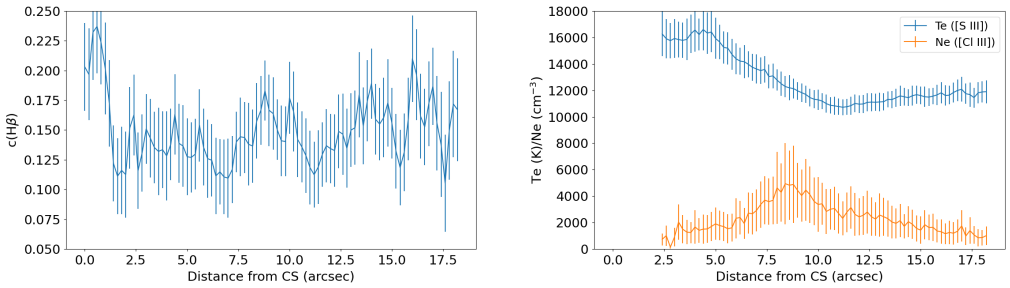

Figure 4.14: Left-panel: c(Hβ), Right-panel: Te([SII]) and Ne([Cl III])

slit's P.A. = 320 degrees

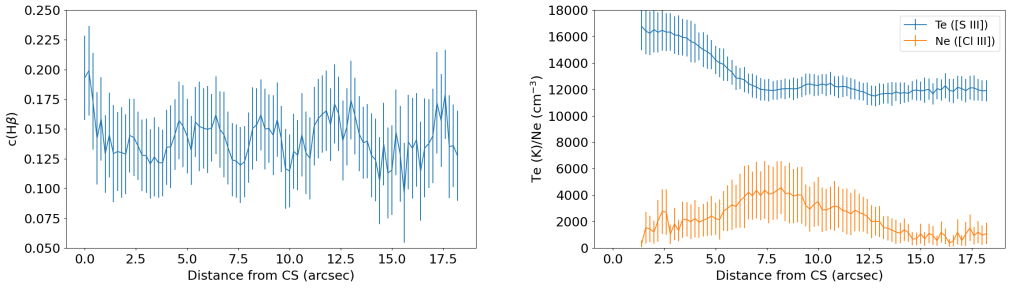

Figure 4.15: Left-panel: c(Hβ), Right-panel: Te([SII]) and Ne([Cl III])

high ($\sim$ 17,000 K) in the inner nebular structures, gradually decreasing, and finally stabilising at approximately 12,000 K in the outer regions of the planetary nebula. On the other hand, the electron density increase at a distance of $\sim$ 8.0" from the CS, in both cases. At this distance, the rim is located.

The radial profiles of several typical emission lines are captured in Figure 4.16, and the corresponding distances from the central star (CS) where each emission line reaches its maximum value are presented in Table 4.1. In every case (for P.A. 160 or 320 degrees), the low ionisation lines of [N II], [C I], [S II] and [O I] peak at the low ionisation structures (see the distances in Table 4.1 and the distance of the LISs in Image 4.13), while the high ionisation lines of Hα and [O III] peak close to the bright rim.

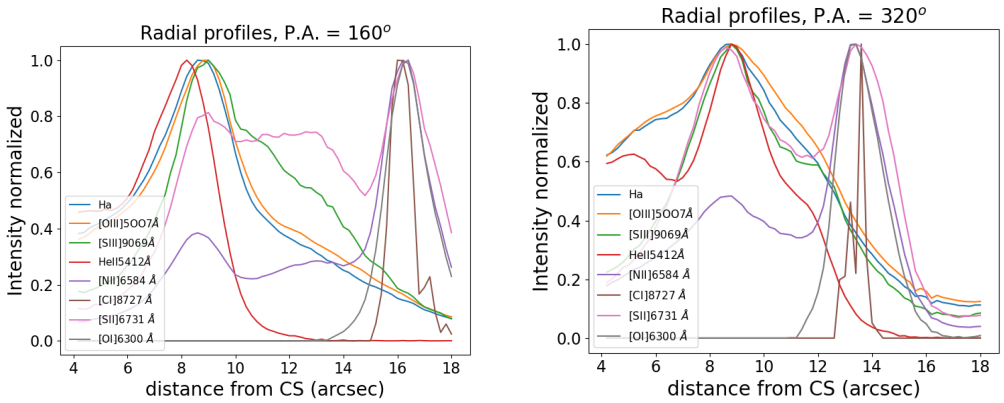

Figure 4.16: Radial profiles for P.A. 160 degrees(Left-panel) and 320 degrees (Right-panel).

Radial profiles		
	P.A.=160^o	P.A.=320^o
Emission line (Å)	peak (arcsec)	peak (arcsec)
Hα	8.6	8.8
[O III] 5007	9.0	8.8
[S III] 9069	9.0	8.8
He II 5412	8.2	8.8
[N II] 6584	16.2	13.4
[C I] 8727	16.0	13.6
[S II] 6731	16.4	13.4
[O I] 6300	16.4	13.4

Table 4.1: The corresponding distances from the central star (CS) where each emission line reaches its maximum value are presented in this table

1.3. Angular analysis

In the case of the angular analysis, the slit's position angle ranges from 0 to 360 degrees, with a step of 10 degrees. The slit was extended from the centre of the nebula to the outer parts with fixed dimensions, 92x10 spaxels.

From Figure 4.17 left panel we can see that the extinction is almost

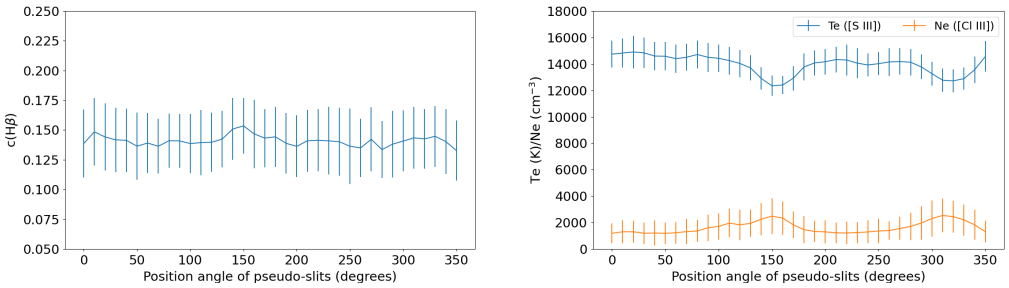

Figure 4.17: Left panel: c(Hβ) as a function of the P.A., Right panel: Te[S III], Ne[Cl III] as a function of the P.A.

constant throughout the nebula with a mean value of 0.13. In the same Figure but in the right panel, we can see that the electron temperature decrease for P.A. 160 and 320 degrees where the LISs are, but the temperature calculated from [S III] is more representative for the inner structures of the nebula. The opposite behaviour is observed for the electron density. In this case, the difference isn't significant.

1.4. 2D analysis

1.4.1. Te, Ne and c(Hβ) 2D maps

The first results of this analysis are about the electron temperature, the electron density and the extinction of NGC 3242. From the c(Hβ) 2D map, Figure 4.18, it is clear that the extinction coefficient is almost constant throughout the nebula, while from the pixel distribution (right-panel) it is concluded once again that the mean value of c(Hβ) is 0.13, which is in good agreement with previous studies (Monreal-Ibero et al., 2005; Pottasch and Bernard-Salas, 2008).

The map of Te([S III]) (Figure 4.19, left-panel) is more representative of the high ionisation regions, while the map of Te([N II]) is more representative of the low ionised regions (Figure 4.19, right-panel). In the first case, the electron temperature is higher at the rims and gradually decreases outwards. While the Te([N II]) is calculated only on the LISs resulting to the temperature map shown in (Figure 4.19). In this case, Te([N II]) reaches 12,000 K, which is in good agreement with the results from previous studies (Krabbe and Copetti, 2006; Pottasch and Bernard-

Salas, 2008; Monteiro et al., 2013). For the median values of Te([N II]) and Te([S III]) see Table 4.2.

Moving to the 2D maps for the electron density, the Figure 4.20 represent Ne([S II]) (left panel) and Ne([Cl III]) (right panel). The electron density Ne([S II]) is calculated only at the position of the LISs which fulfil the criteria of the mask. Ne([Cl III]) map shows that the electron density is higher at the nebular rim but overall, there is no significant variation from the inner to the outer parts of the nebula. In Table 4.2 the median values for the electron density are presented.

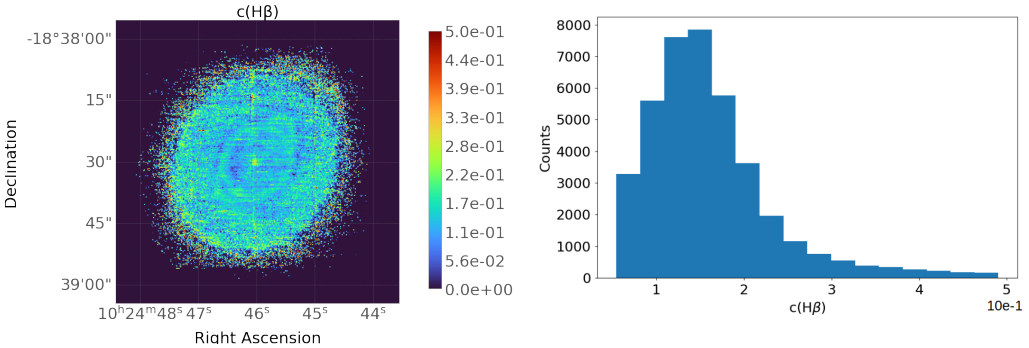

Figure 4.18: The 2D map of the extinction coefficient is shown in the left panel, while the right panel shows the pixel distribution of c(Hβ) map.

Median values Te, Ne		
Te(K) / Ne(cm^{-3})	median value	standard deviation
Te([N II])	12,200	1,560
Te([S III])	11,900	1,660
Ne([S II])	1,590	938
Ne([Cl III])	1,620	1,220

Table 4.2: In this table, we can see the median values for the electron temperature and electron density.

Electron Temperature maps

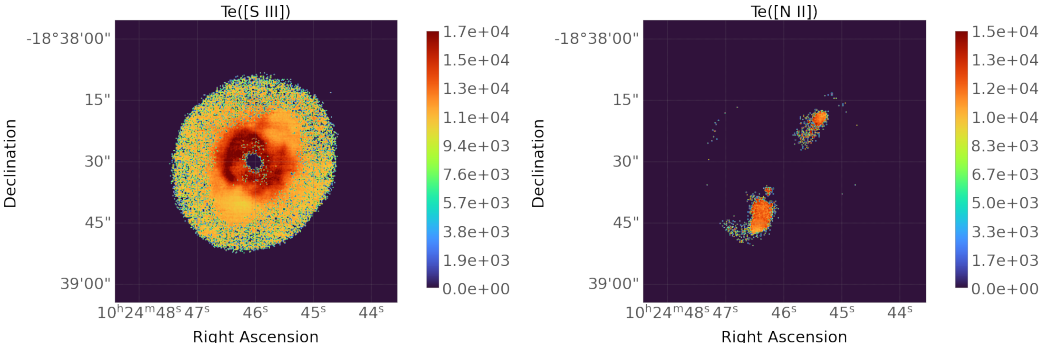

Figure 4.19: Left pane: Te([S III]) given the electron density calculated from [Cl III], Right panel: Te([N II]) given the electron density calculated from [S II].

Electron Density maps

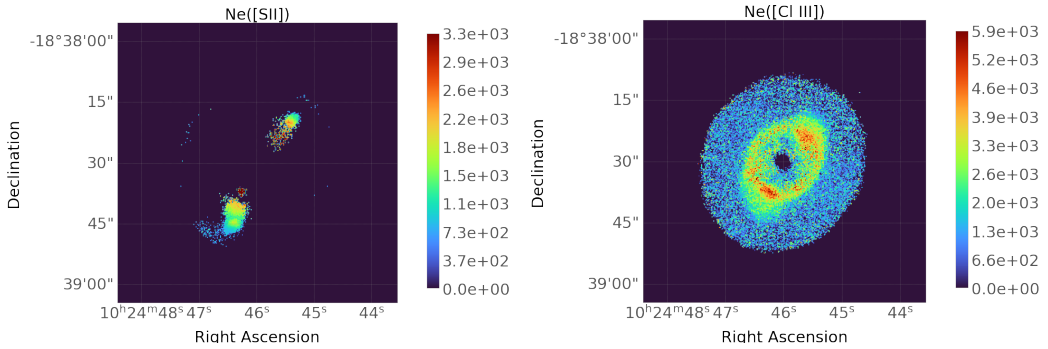

Figure 4.20: Left pane: Ne([S II]) given the electron temperature Te([N II]), Right panel: Ne([Cl III]) given the electron temperature Te([S III]).

1.4.2. Ionic and Elemental abundances

Figure 4.21 (left panel) displays the He/H. The He++(5412 Å)/H+ is concentrated at the inner nebular structures while the He+(5876 Å)/H+ is measured only at the LISs, because in the second case Te([N II]) was used. This explains the structure that we observe in the elemental abundance of Helium. In the case of N/H (right panel) for every ionic

abundance Te([N II]) has been used, leading to the calculation of the elemental abundance only at the LISs. In more detail, Table 4.3 displays the electron temperature (Te) and electron density (Ne) values that are used for calculating the ionic abundances of each element.

Ionic abundances	Te(K)	Ne(cm^{-3})
He+/H+	[N II]	[S II]
He++/H+	[S III]	[Cl III]
O/H+	[N II]	[S II]
O+/H+	[N II]	[S II]
O++/H+	[S III]	[Cl III]
N/H+	[N II]	[S II]
N+/H+	[N II]	[S II]
S+/H+	[N II]	[S II]
S++/H+	[S III]	[Cl III]
Ar++/H+	[S III]	[Cl III]
Ar++/H+	[S III]	[Cl III]
Ne++/H+	[S III]	[Cl III]
Cl+/H+	[N II]	[S II]
Cl++/H+	[S III]	[Cl III]
Cl+++/H+	[S III]	[Cl III]

Table 4.3: This table provides the values of Te and Ne that are used for the calculation of each ionic abundance.

Moving to the Figure 4.22 in the left-panel the O/H is presented as it was calculated from our analysis. The elemental abundance of Oxygen is calculated via the relation:

$$A(O) = ICF(O)(O^{+} + O^{++})/H^{+}, \tag{4.1}$$

where O++/H+ is calculated in every nebular structure, unlike O+/H+ which is calculated only at the LISs (see Figure 4.23). The ICF from Alexander and Balick (1997) in this case is given as a function of Helium ions,

$$ICF(O) = \left(\frac{He^{+} + He^{++}}{He^{+}}\right)^{2/3} \tag{4.2}$$

However, as it was mentioned before, He+/H has non-zero values only at the LISs. So in every other case, the denominator of 4.2 is zero. Finally, when 4.2 is plugging into 4.1 it returns O/H only at the LISs.

For a direct comparison, we also present the O/H from Monteiro et al. (2013) (Figure 4.22, right panel). In this case, the O/H is calculated in the whole nebula, unlike our analysis. Nevertheless, in this study VIMOS data were used and while VIMOS configuration does not include either the [O II] 3727 Å or the 7325 Å emission lines, the map O+/H+ cannot be calculated. To solve this problem, Monteiro et al. (2013) generated these maps by using values from the literature and assuming that there is no variation of these abundances throughout the PN. Also, the electron temperature that was used in this study was calculated from [O III]. The above may reflect that in our analysis the O/H is probably better determined as the [O II] 7325 Å emission line was available in our dataset, and we also used for the low ionisation ions the Te([N II]) which is more representative.

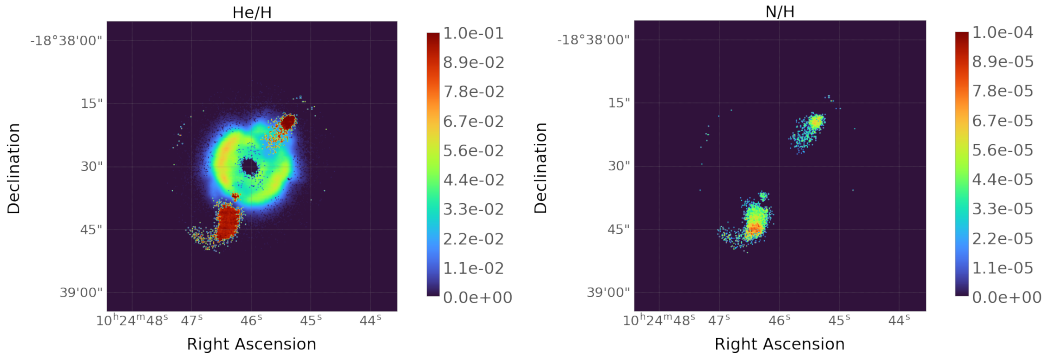

Figure 4.21: 2D maps of some elemental abundances, Left-panel: He/H, Right-panel: N/H.

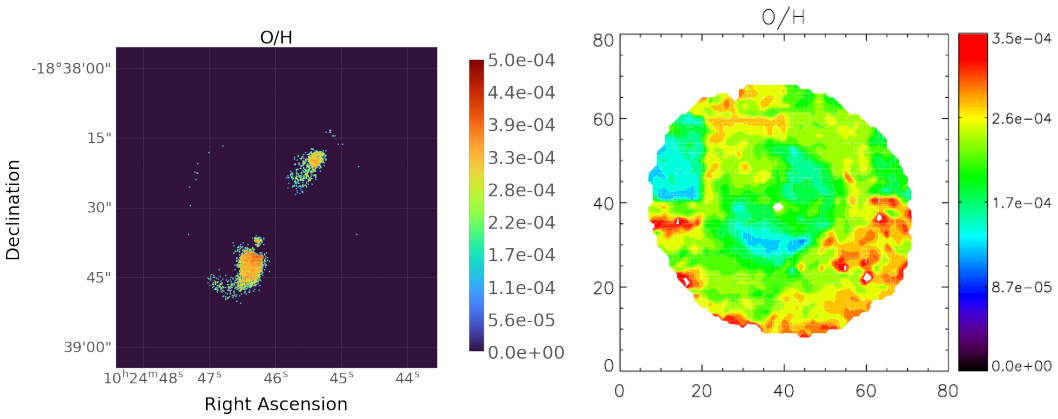

Figure 4.22: Left-panel: O/H 2D map calculated from SATELLITE, Right-panel: O/H 2D map from Monteiro et al. (2013).

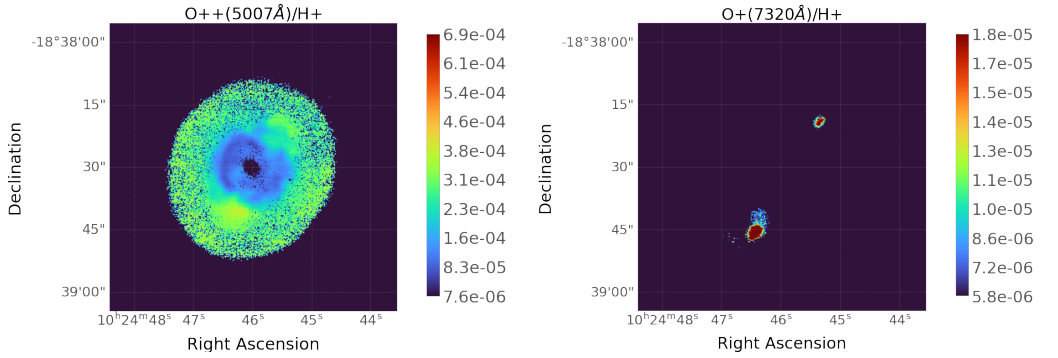

Figure 4.23: Left-panel: O++(5007 Å)/H+ 2D map, Right-panel: O+(7320 Å)/H+ 2D map from.

1.4.3. Emission line ratios and shock excitation

The emission line ratios [N II]/Hα and [S II]/Hα emphasise the degree of ionisation, and the criterion [S II]/Hα $>$ 0.4 has been used for the identification of shock excited regions, e.g. Kopsacheili et al. (2019).

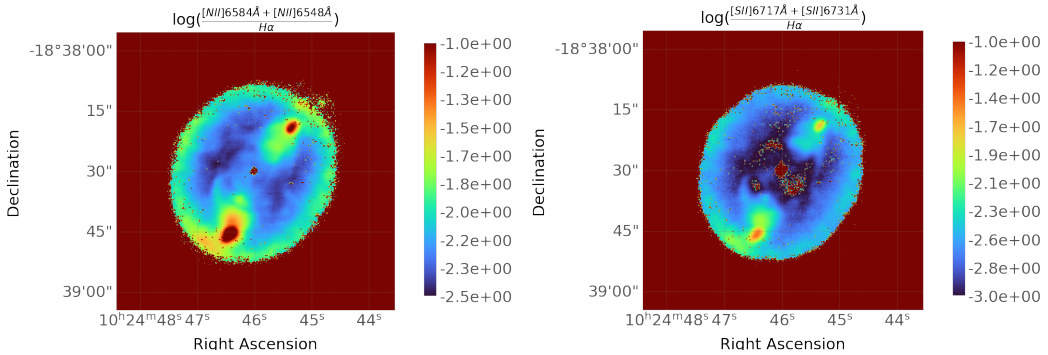

Figure 4.24: 2D maps of the emission line ratios Left panel: log([N II]/Hα), Right panel: log([S II]/Hα)

If this criterion is satisfied, a shock excitation process may be active. From Figure 4.24 it is obvious that LISs' ionisation level is lower than the rest of the PN's structures, as it was expected. Also, it is important to note that the aforementioned shock criterion isn't satisfied. In addition, the [N II]/[O III] ratio (Figure 4.25) represents the ionisation level as well. This ratio takes small values for the high ionization regions, while the opposite happens for the low ionization ones.

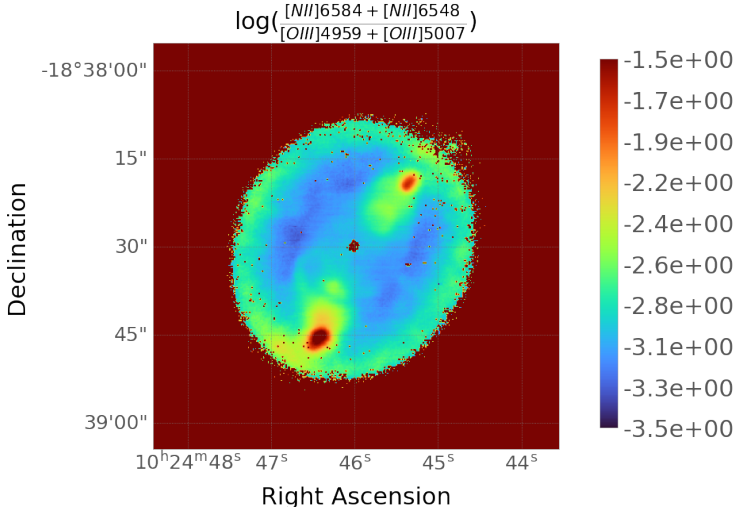

Figure 4.25: The logarithmic emission line ratio [N II]/Hα 2D map

The ratio [O III]/Hα it has been also used for the search of shock

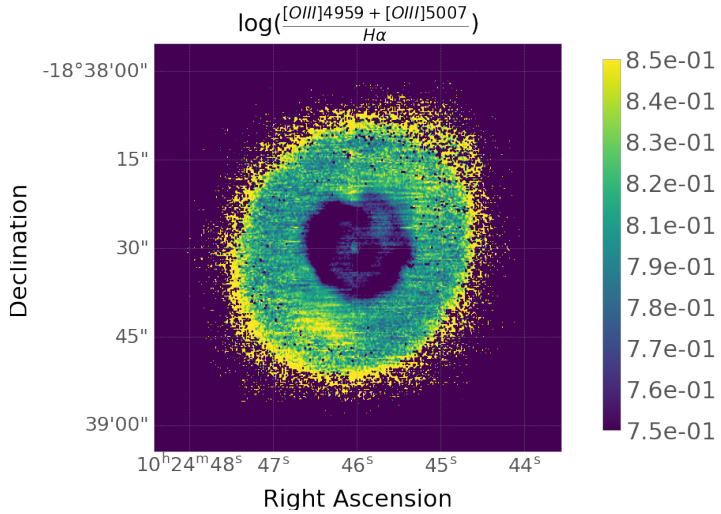

Figure 4.26: 2D map of the emission line ratio log([O III]/Hα)

fronts in planetary nebulae. Guerrero et al. (2013) suggested that shock fronts can be generated if a dense shell expands into a less dense medium. The main assumption is that a shock front would cause local increase of the electron temperature and since the [O III] is highly temperature dependent, we expect that these regions would be enriched with [O III] emission. At the same time, the lower density would decrease the emissivity of Hα, since this emission line is more sensitive to the electron density. As a result, it is anticipated that there will be a region located in front of the shock, at the tip of a collimated outflow, where the [O III]/Hα ratio is noticeably increased (Guerrero et al., 2013).

Another mechanism that would cause shock fronts and the enhancement of [O III]/Hα, is the expansion of the different nebular shells. There are two distinct regions where these phenomena occur: one at the leading edge of the outer shell, propagating into the unperturbed AGB wind, and another at the leading edge of the bright rim, expanding into the outer shell. In Figure 4.26 only one shell is captured (yellow ring). However, Guerrero et al. (2013) argued that two shock fronts are present based on the HST data. We don't confirm the enhancement of [O III]/Hα in the inner shell.

Lastly, from the [O I]/Hα map, we can see that the [O I] line is only emitted at the LISs. Figure 4.27 shows the variation of the [O I]/Hα line within the LISs. More specific, [O I]/Hα takes higher values at the centre and gradually decreases.

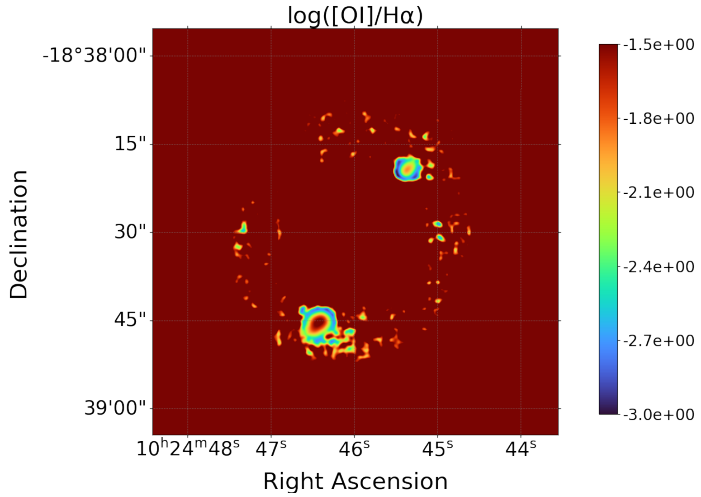

Figure 4.27: Smoothed 2D map of the emission line ratio log([O I]/Hα)

1.4.4. The identification of [C I] 8727 Å emission line

Last but not least, our analysis revealed the existence of the far-red atomic [C I] 8727 Å emission line originate only from the LISs. Figure 4.28 displays the logarithmic ratio [C I]/Hα while Figure 4.29 shows the emission line map. This finding in conjunction with the enhanced low-ionisation lines such as [N II], [S II], [O I] implies a partially ionised gas which may surround a dense molecular gas. The presence of [C I] at the LIS provide further support on the scenario in which LISs are mini-photo-dissociation regions (PDRs) embedded in PNe. [C I] has already been detected in PDRs of HII regions. The existence of atomic C and atomic O at the LISs may imply the dissociation of CO.

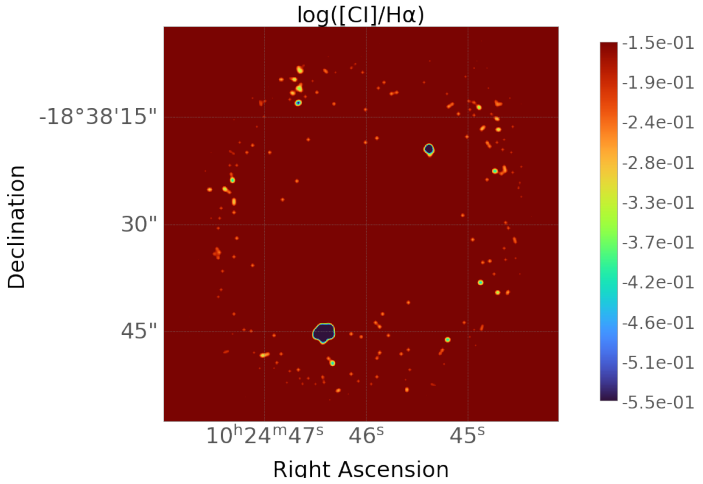

Figure 4.28: Smoothed 2D map of the emission line ratio log([C I]/Hα)

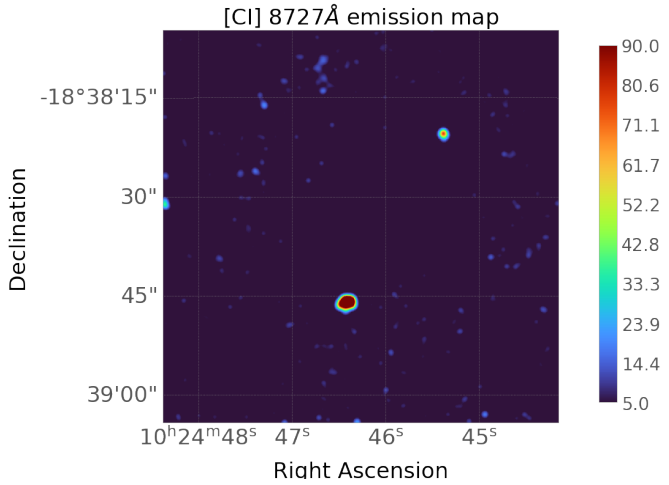

Figure 4.29: Smoothed emission line map of [C I] 8727Å. For this figure, logarithmic and min/max scales have been used.

1.4.5. Diagnostic diagrams

Except of the 2D maps, diagnostic diagrams are also presented here. As previously mentioned in the preceding chapter, the diagnostic diagrams serve to compare the relative line intensity ratios of certain emission lines commonly observed in planetary nebulae (PNe), supernova remnants (SNR), and HII regions. Figures 4.30 and 4.31 display the regions where each nebula is expected to fall. To perform a direct comparison between

1D and 2D analysis, SATELLITE ran the following modules together: 2D analysis, specific slit analysis and radial analysis.

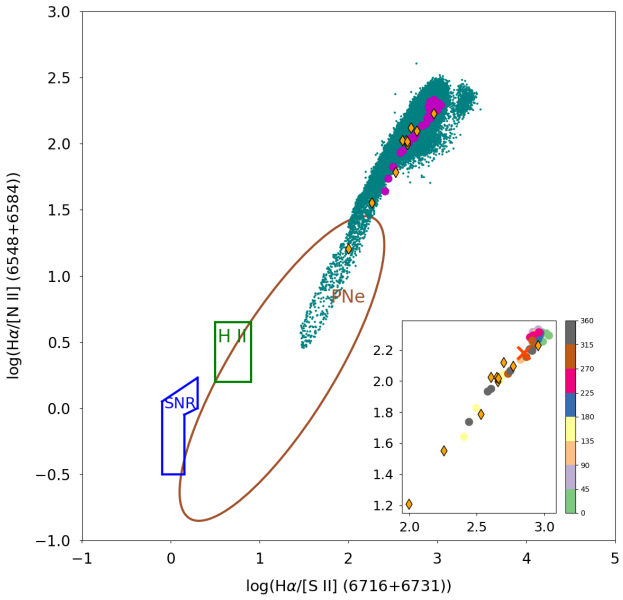

Figure 4.30: Diagnostic diagram Hα/[N II] versus Hα/[S II]. Cyan dots: values of individual pixels Pink circles: values obtained from the angular analysis task Yellow diamonds: values from the 10 simulated slits in the specific slits task

As a result, the ratios extracted from each module are drawn together on the diagnostic diagrams. The slits that were used for the specific slit module are presented in Figure 3.5. At this point it is important to mention that at first these diagrams were created based on data obtained from 1D slit spectroscopy, so the results for the 2D analysis aren't fully representative. In Figure 4.30, unlike the Figure 4.31, we can see that the ratios have lower values than the expected ones for a PN, thus the resulted values are mainly outside the PNe region (orange ellipse). This behaviour indicates that NGC 3242 is overall a low ionised nebula. However, there are some pixel values that are closer to the expected ones for PN, and these are probably coming from the inner nebular structures.

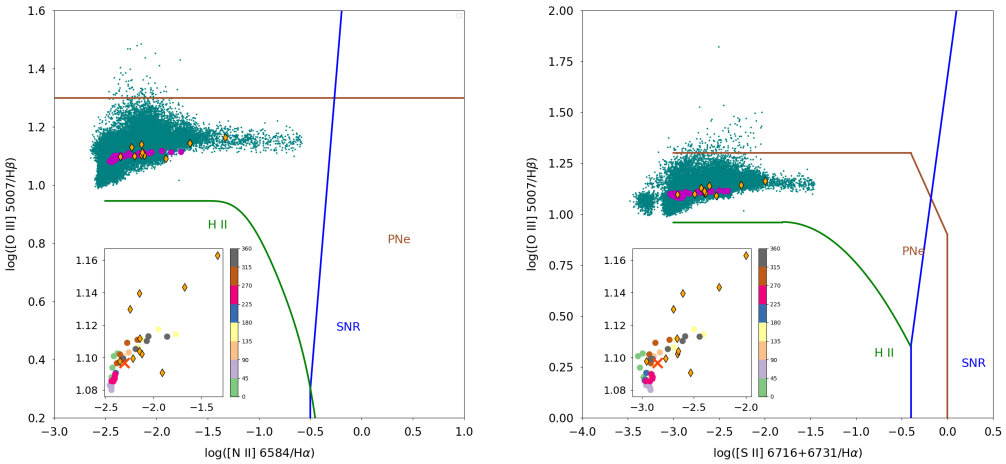

Figure 4.31: Left panel: log([O III]/Hβ) versus log([N II]/Hα), Right panel: log([O III]/Hβ) versus log([N II]/Hα). Cyan dots: values of individual pixels Pink circles: values obtained from the angular analysis task Yellow diamonds: values from the 10 simulated slits in the specific slits task

2. Spitzer Infrared data

In Figure 4.32, the profiles of IRAC channels are presented. The radial analysis was carried out for P.A. 160^o and 320^o passing through the centre of the nebula to the LISs. The aim of this task was the detection of potential infrared emission at the position of LISs. We can see that the emission at 8 μm is stronger at every position relatively to the other bands, while the fluxes at 3.6 μm and 5.8 μm are almost the same. In every case, the peak is observed at the position of the bright rim. The same behaviour is observed for P.A. = 320^o, only in this case the peak isn't so sharp, probably because the rim isn't so bright.

Moving to the figure 4.33, we can see the ratios 3.6 μm/4.5 μm, 5.8 μm/4.5 μm and 8.0 μm/4.5 μm. With dashed lines it is noted the position of the LISs based on MUSE observations. Phillips et al. (2010) found lower values (indicated as "deep" on the figures) of the ratios at the position of the LISs in the planetary nebula NGC 7009. They found that this decrease in the ratios is associated with an increase in emission

from the 4.5 μm band. The primary emission in this band is likely H_2 (Akras et al., 2020). However, in the case of NGC 3242, the LISs were not detected with IRAC. This observation suggests that the emission from H_2 is either faint or absent altogether. However, further investigation is required to confirm this hypothesis.

We can see that in every case the ratios take the smaller values at the rim and increase to the outer nebular structures. One possible explanation for the higher values of the ratios as we move towards the halo region is the potential significance of dust and continuum emission. Within the 5.8 μm band the continuum is strong and it becomes even stronger in 8.0 μm channel. The dominant contribution to longer wave mid-infrared IRAC fluxes is probably due to this factor. At the same time, the H_2 lines may also contribute at 5.8 and 8.0 IRAC bands (Akras et al., 2017). It is likely that the 8.0 μm wavelength also contains a dust band that has a peak at 7.48 μm (Phillips et al., 2009). This peak is potentially blended with the [Na III] emission line at λ 7.319 μm.

Radial profiles

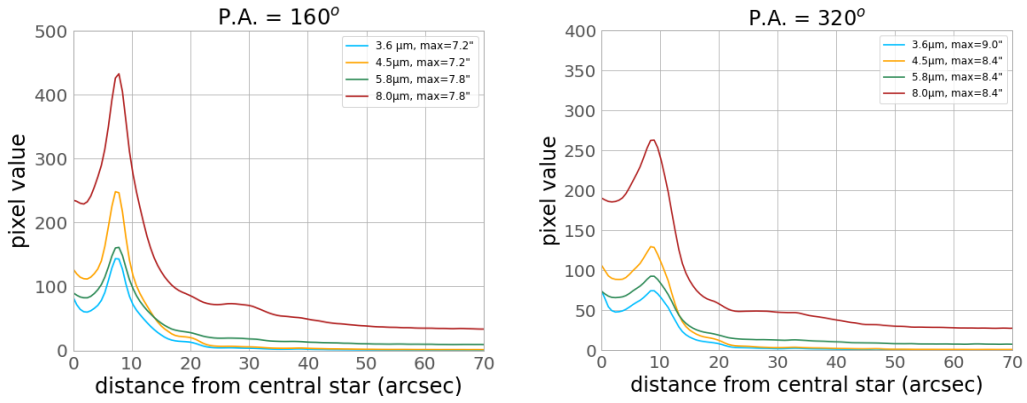

Figure 4.32: Surface brightness profiles of IRAC bands

In Figure 4.34 three rings are visible around the main body of NGC 3242 with approximate angular sizes 30, 39 and 57 arcsec. Given that the distance of NGC 3242 from Gaia Early Data Release 3 (EDR3) (Bailer-Jones et al., 2021) is approximately $1,279^{+63}_{-62}$ pc, we can compare the kinematic age of these rings by simply divide their size with the expansion velocity. Assuming a constant expansion velocity 23 km/s (Phillips et al., 2009) the age of each ring can be found. The results are listed in Table 4.4. It is concluded that these rings weren't created at the same time,

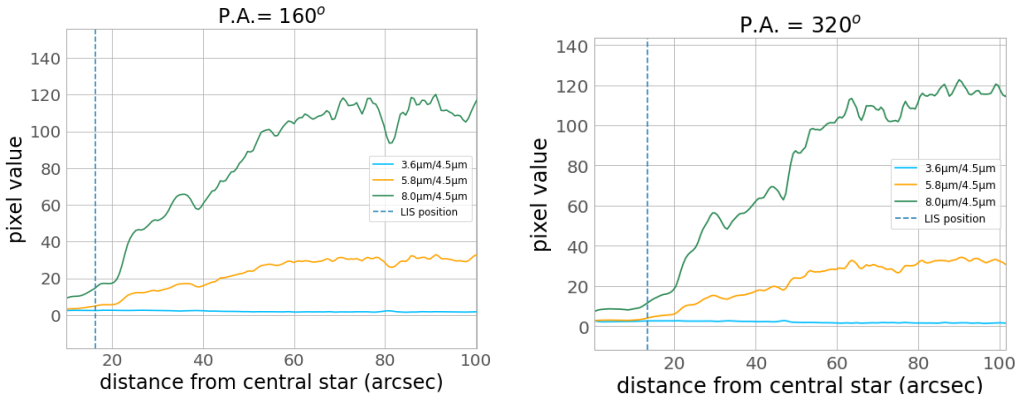

Figure 4.33: Flux ratios of IRAC bands in comparison to the 4.5μm band. With dashed lines the expected position of LISs, based on MUSE observations, is marked on the figure.

which means that they are probably related to different mass loss episodes during the AGB phase.

Nebular rings		
Rings	Angular size (arcsec)	Kinematic age (yr)
1st	30 ± 0.6	$8,002^{+1,631}_{-1,627}$
2nd	39 ± 0.6	$10,390^{+1,664}_{-1,657}$
3rd	57 ± 0.6	$14,945^{+1,702}_{-1,735}$

Table 4.4: In this table, the angular sizes and the ages of the three rings of NGC 3242 are listed.

Lastly, in Figures 4.35 and 4.36 the ratios of IRAC bands are presented in 2D maps. In every case, it is obvious that the ratios decrease towards the outer structures. Also, in every case the rings are faintly discernible, and the ratios there are lower than the ones of the halo that they're embedded in. This result may indicate that these rings are dusty because of the various mass loss episodes that resulted in their formation. Except of the rings, in Figure 4.36 it is observed a clumpy structure which surrounds the halo. These fuzzy regions can arise from interactions of the gas with the ISM, or they may be the outcome of mass loss events from the central star. In the case of NGC 3242 their emission is stronger at the 5.8 μm and 8.0 μm bands. This may indicate either a dusty composition

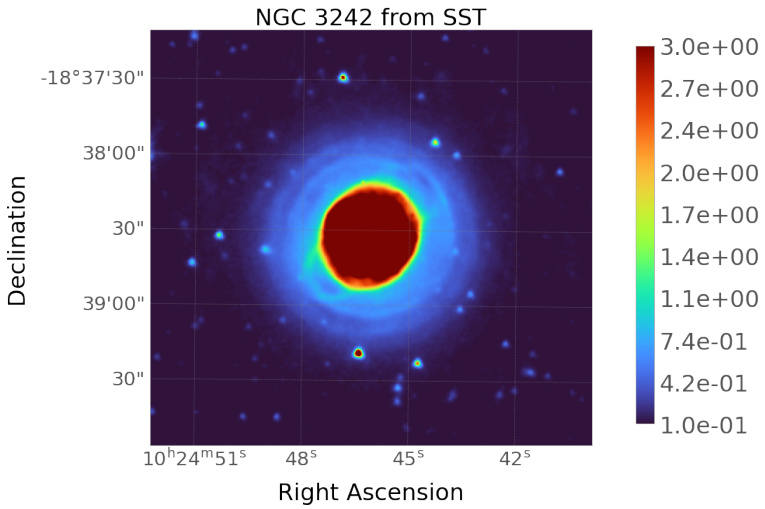

Figure 4.34: Three rings are observed based on SST/IRAC observations. Min/max and logarithmic scale were applied.

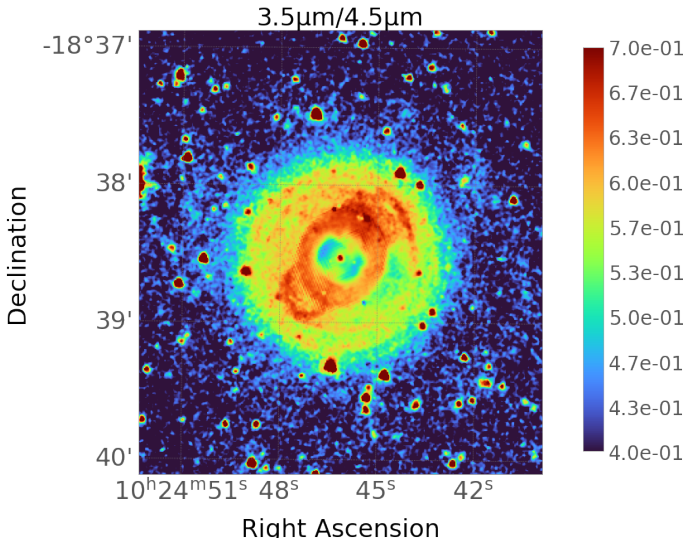

Figure 4.35: The ratio 3.5 μm/4.5 μm in the form of 2D map. Min/max and logarithmic scale were applied for this map.

or a rich H_2 gas.

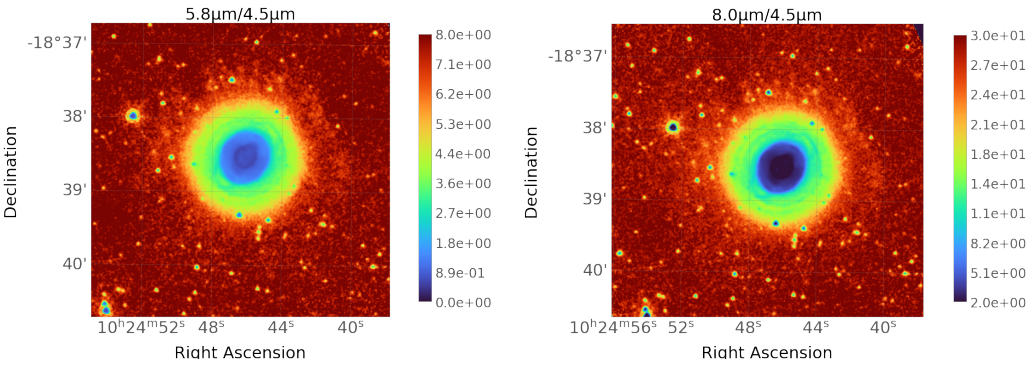

Figure 4.36: The ratios 5.8 μm/4.5 μm (Left panel) and 8.0 μm/4.5 μm (Right panel) in the form of 2D map. Min/max and logarithmic scale were applied for this maps

Chapter 5

Summary and Conclusions

Planetary nebulae are created during the last evolutionary stages of low-to-intermediate mass stars. The most common scenario about their origin is the Interacting Stellar Wind (ISW) model. The concept of ISW model, proposed by Kwok et al. in 1978, suggests that planetary nebulae (PNe) are formed through the interaction between intense stellar winds and material expelled from low-mass stars during the asymptotic giant branch (AGB). This suggests that PNe do not result from a single instance of mass loss, but rather they represent the redistribution of material ejected over an extended duration.

The colourful halo of gas, which surrounds the dying star, is the material that was originated from the star itself but has been expelled. The planetary nebula is glowing due to the ultraviolet radiation emitted by the central star. By this procedure different structures are created like halo, shells or bright edged structures called rims. All of them, are well studied and there are a lot known about their origin. So, the biggest enigma is around the microstructures known as Low Ionisation Structures (LISs) that are observed in some planetary nebulae.

Planetary nebulae offer unique opportunities for studying the material that once was part of a star. By studying the nebula's chemical composition, we can gain insights into the constituent materials from which the star initially formed. Additionally, the abundance of specific elements, such as Carbon and Nitrogen, within the nebula provides valuable information about the physical processes that occurred within the star during its lifetime of nuclear fusion. The study of planetary nebulae contributes

to our understanding of how stars undergo transformations, or evolve, throughout their lifetimes.

The aim of this thesis was the spectroscopic analysis of the planetary nebula NGC 3242, which contains LISs. This nebula has never been studied with MUSE IFU data before. For our analysis, SATELLITE python code was used. We found that the electron temperature decrease from the inner to the outer structures of the nebula (calculated from [S III]), while the electron density is higher at the nebular rim. At the same time, some ionic abundances present variation from the inner structures to the LISs, but overall there is no significant chemical variation throughout the nebula. It is important to mention that the abundances are affected by the masking on the emission line maps. For the low ionisation ions, which require the use of Te([N II]) for abundance calculations, either the abundances were not calculated near the nebular centre or the calculations resulted in highly uncertain values. Therefore, in the study of the chemical composition of this particular planetary nebula, it is important to consider the faint emission of certain lines in the inner structures. This problem must be resolved out in order to calculate elemental abundances in the whole PN.

The extinction coefficient is almost constant with mean value c(Hβ)=0.13 and the diagnostic diagrams revealed that NGC 3242 is a low ionised nebula. In addition, it is concluded that the LISs have intense emission of the low ionisation lines such as [N II], [S II] or [O I]. Also, through a thorough investigation of the available data, we detected the line atomic line of [C I] 8727 Å emitted only from the LISs. The existence of Carbon has been previously connected to the existence of H_2. So this result may imply that LISs are formed by a neutral gas. In a future work, I would like to be able to observe this NGC 3242 with a H_2 filter to test if the aforementioned assumption is right. Taking a step further, it would be highly valuable to conduct a comprehensive statistical analysis of a larger sample of PNe that exhibit LISs. This would allow for a thorough investigation of their physical parameters and provide insights into the existence of H_2.

Last but not least, we used the available infrared image data from SST/IRAC to carry out a multi-wavelength analysis. Through our analysis we identified three ring-like structures around the main body of the PN which may represent the result of different mass-loss episodes during the AGB phase. Unfortunately, the LISs weren't detected from IRAC, so we couldn't take more information about them from Spitzer data.

References

Akras, S. (2010). *Detection and study of phenomena in interstellar matter*. PhD thesis, Univesity of Patras and National Observatory of Athens.

Akras, S. and Gonçalves, D. R. (2016). Low-ionization structures in planetary nebulae – I. Physical, kinematic and excitation properties . *Monthly Notices of the Royal Astronomical Society*, 455(1):930–961.

Akras, S., Gonçalves, D. R., and Ramos-Larios, G. (2017). H2 in low-ionization structures of planetary nebulae. *Monthly Notices of the Royal Astronomical Society*, 465(2):1289–1296.

Akras, S., Gonçalves, D. R., Ramos-Larios, G., and Aleman, I. (2020). H2 emission in the low-ionization structures of the planetary nebulae NGC 7009 and NGC 6543. *Monthly Notices of the Royal Astronomical Society*, 493(3):3800–3810.

Akras, S., Guzman-Ramirez, L., Leal-Ferreira, M. L., and Ramos-Larios, G. (2019). A Census of Symbiotic Stars in the 2MASS, WISE, and Gaia Surveys. , 240(2):21.

Akras, S., Monteiro, H., Walsh, J., Isabel, A., Gonçalves, D. R., and Boumis, P. (2022). SATELLITE: Application to Planetary Nebulae IFU Data. *Galaxies*, 10(1):27.

Alexander, J. and Balick, B. (1997). Nebular abundance errors. *The Astronomical Journal*, 114:713–721.

Allington-Smith, J. (2006). Basic principles of integral field spectroscopy. *New Astronomy Reviews*, 50(4):244–251. Integral Field Spectroscopy: Techniques and Data Production.

Bacon, R., Accardo, M., Adjali, L., Anwand, H., Bauer, S., Biswas, I., Blaizot, J., Boudon, D., Brau-Nogue, S., Brinchmann, J., Caillier, P., Capoani, L., Carollo, C. M., Contini, T., Couderc, P., Daguisé, E., Deiries, S., Delabre, B., Dreizler, S., Dubois, J., Dupieux, M., Dupuy,

C., Emsellem, E., Fechner, T., Fleischmann, A., François, M., Gallou, G., Gharsa, T., Glindemann, A., Gojak, D., Guiderdoni, B., Hansali, G., Hahn, T., Jarno, A., Kelz, A., Koehler, C., Kosmalski, J., Laurent, F., Le Floch, M., Lilly, S. J., Lizon, J. L., Loupias, M., Manescau, A., Monstein, C., Nicklas, H., Olaya, J. C., Pares, L., Pasquini, L., Pécontal-Rousset, A., Pelló, R., Petit, C., Popow, E., Reiss, R., Remillieux, A., Renault, E., Roth, M., Rupprecht, G., Serre, D., Schaye, J., Soucail, G., Steinmetz, M., Streicher, O., Stuik, R., Valentin, H., Vernet, J., Weilbacher, P., Wisotzki, L., and Yerle, N. (2010). The MUSE second-generation VLT instrument. In McLean, I. S., Ramsay, S. K., and Takami, H., editors, *Ground-based and Airborne Instrumentation for Astronomy III*, volume 7735 of *Society of Photo-Optical Instrumentation Engineers (SPIE) Conference Series*, page 773508.

Bailer-Jones, C. A. L., Rybizki, J., Fouesneau, M., Demleitner, M., and Andrae, R. (2021). VizieR Online Data Catalog: Distances to 1.47 billion stars in Gaia EDR3 (Bailer-Jones+, 2021). *VizieR Online Data Catalog*, page I/352.

Balick, B., Alexander, J., Hajian, A. R., Terzian, Y., Perinotto, M., and Patriarchi, P. (1998). FLIERs and Other Microstructures in Planetary Nebulae. IV. Images of Elliptical PNs from the Hubble Space Telescope. , 116(1):360–371.

Barria, D. and Kimeswenger, S. (2018). HST/WFPC2 imaging analysis and cloudy modelling of the multiple-shell planetary nebulae NGC 3242, NGC 6826, and NGC 7662. *Monthly Notices of the Royal Astronomical Society*, 480(2):1626–1638.

Corradi, R. L. M., Sánchez-Blázquez, P., Mellema, G., Gianmanco, C., and Schwarz, H. E. (2004). Rings in the haloes of planetary nebulae. , 417:637–646.

Corradi, R. L. M., Schönberner, D., Steffen, M., and Perinotto, M. (2003). Ionized haloes in planetary nebulae: new discoveries, literature compilation and basic statistical properties. , 340(2):417–446.

Danehkar, A. (2022). Morphologies of wolf–rayet planetary nebulae based on IFU observations. *Galaxies*, 10(2):45.

Fang, X., Zhang, Y., Kwok, S., Hsia, C.-H., Chau, W., Ramos-Larios, G., and Guerrero, M. A. (2018). Extended structures of planetary nebulae detected in h2 emission. *The Astrophysical Journal*, 859(2):92.

Fitzpatrick, E. L. (1999). Correcting for the effects of interstellar extinction. *Publications of the Astronomical Society of the Pacific*, 111(755):63.

García-Rojas, J., Morisset, C., Jones, D., Wesson, R., Boffin, H. M. J., Monteiro, H., Corradi, R. L. M., and Rodríguez-Gil, P. (2021). MUSE spectroscopy of planetary nebulae with high abundance discrepancies. *Monthly Notices of the Royal Astronomical Society*, 510(4):5444–5463.

García-Segura, G., Langer, N., Różyczka, M., and Franco, J. (1999). Shaping bipolar and elliptical planetary nebulae: Effects of stellar rotation, photoionization heating, and magnetic fields. *The Astrophysical Journal*, 517(2):767.

Goncalves, D. R., Ercolano, B., Carnero, A., Mampaso, A., and Corradi, R. L. M. (2006). On the nitrogen abundance of fast, low-ionization emission regions: the outer knots of the planetary nebula NGC 7009. *Monthly Notices of the Royal Astronomical Society*, 365(3):1039–1049.

Gonçalves, D. R., Corradi, R. L. M., and Mampaso, A. (2001). Low-Ionization Structures in Planetary Nebulae: Confronting Models with Observations. , 547(1):302–310.

Gonçalves, D. R., Mampaso, A., Corradi, R. L. M., and Quireza, C. (2009). Low-ionization pairs of knots in planetary nebulae: physical properties and excitation. *Monthly Notices of the Royal Astronomical Society*, 398(4):2166–2176.

Guerrero, M. A., Toalá, J. A., Medina, J. J., Luridiana, V., Miranda, L. F., Riera, A., and Velázquez, P. F. (2013). Unveiling shocks in planetary nebulae. *Astronomy &amp Astrophysics*, 557:A121.

Gómez-Muñoz, M. A., Blanco Cárdenas, M. W., Vázquez, R., Zavala, S., Guillén, P. F., and Ayala, S. (2015). Morpho-kinematics of the planetary nebula NGC 3242: an analysis beyond its multiple-shell structure. *Monthly Notices of the Royal Astronomical Society*, 453(4):4175–4184.

Hajian, A. R., Balick, B., Terzian, Y., and Perinotto, M. (1997). Fliers and other microstructures in planetary nebulae. iii. *The Astrophysical Journal*, 487(1):304.

Hannu Karttunen, Pekka Kröger, H. O. M. P. K. J. D. (2017). *Fundamental Astronomy*. Springer-Verlag Berlin Heidelberg, ISBN: 978-3-662-53044-3, ISBN: 978-3-662-53045-0 (eBook), doi: 10.1007/978-3-662-53045-0.

H.Shu, F. (2017). *The Physical Universe: An Introduction to Astronomy*. University Science Books.

Kaler, J. B. (2020). *Stellar evolution*. AccessScience, McGraw Hill. doi:10.1036/1097-8542.654000, [accessed 2023 Mar 13]. https://www.accessscience.com/content/article/a654000.

Kopsacheili, M., Zezas, A., and Leonidaki, I. (2019). A diagnostic tool for the identification of supernova remnants. *Monthly Notices of the Royal Astronomical Society*, 491(1):889–902.

Krabbe, A. C. and Copetti, M. V. F. (2006). Chemical abundances in seven galactic planetary nebulae. , 450(1):159–166.

Kwok, S. (2000). *The Origin and Evolution of Planetary Nebulae*. Cambridge University Press.

López, J. and Riesgo, H. (2006). Revised diagnostic diagrams for planetary nebulae. *Revista Mexicana de Astronomía y Astrofísica*, 42.

Meaburn, J., López, J. A., and Noriega-Crespo, A. (2000). The complex environment of the high-excitation planetary nebula ngc 3242. *The Astrophysical Journal Supplement Series*, 128(1):321.

Miller, T. R., Henry, R. B. C., Balick, B., Kwitter, K. B., Dufour, R. J., Shaw, R. A., and Corradi, R. L. M. (2016). Analysis of co-spatial uv-optical hst/stis spectra of planetary nebula ngc 3242*. *The Astrophysical Journal*, 830(1):9.

Monreal-Ibero, A., Roth, M. M., Schönberner, D., Steffen, M., and Böhm, P. (2005). Integral field spectroscopy of faint halos of planetary nebulae. *The Astrophysical Journal*, 628(2):L139.

Monteiro, H., Gonçalves, D. R., Leal-Ferreira, M. L., and Corradi, R. L. M. (2013). Spatially resolved physical and chemical properties of the planetary nebula NGC 3242. , 560:A102.

Phillips, J. P., Cuesta, L. C., and Ramos-Larios, G. (2010). Mapping and spectroscopy of the planetary nebula NGC 7009 in the visual and infrared. *Monthly Notices of the Royal Astronomical Society*, 409(3):881–902.

Phillips, J. P., Ramos-Larios, G., Schröder, K.-P., and Contreras, J. L. V. (2009). Rings and haloes in the mid-infrared: the planetary nebulae NGC 7354 and NGC 3242. *Monthly Notices of the Royal Astronomical Society*, 399(3):1126–1144.

Pottasch, S. R. and Bernard-Salas, J. (2008). Abundances of planetary nebulae NGC 3242 and NGC 6369. *Astronomy &amp Astrophysics*, 490(2):715–724.

Reimers, C., Dorfi, E. A., and Höfner, S. (2000). Shaping of elliptical planetary nebulae. The influence of dust-driven winds of AGB stars. , 354:573–578.

Schönberner, D., Balick, B., and Jacob, R. (2018). Expansion patterns and parallaxes for planetary nebulae. , 609:A126.

Torres-Peimbert, S. (2015). Chemical composition of planetary nebulae: The abundance discrepancy problem. *AIP Conference Proceedings*, 1697(1). 040003.

Tsamis, Y. G., Barlow, M. J., Liu, X.-W., Danziger, I. J., and Storey, P. J. (2003). A deep survey of heavy element lines in planetary nebulae – I. Observations and forbidden-line densities, temperatures and abundances. *Monthly Notices of the Royal Astronomical Society*, 345(1):186–220.

Ueta, T. and Otsuka, M. (2021). Proper plasma analysis practice (PPAP), an integrated procedure of extinction correction and plasma diagnostics: A demo with an HST/WFC3 image set of NGC 6720. *Publications of the Astronomical Society of the Pacific*, 133(1027):093002.